CELL BIOLOGY

ER-mitochondria tethering by PDZD8 regulates Ca^{2+} dynamics in mammalian neurons

Yusuke Hirabayashi,[1,2,3,4]* Seok-Kyu Kwon,[1,2,3]* Hunki Paek,[1,2,3] Wolfgang M. Pernice,[5] Maëla A. Paul,[1,2,3] Jinoh Lee,[1,2,3] Parsa Erfani,[1,2,3] Ashleigh Raczkowski,[7] Donald S. Petrey,[8,9] Liza A. Pon,[5,6] Franck Polleux[1,2,3]†

Interfaces between organelles are emerging as critical platforms for many biological responses in eukaryotic cells. In yeast, the ERMES complex is an endoplasmic reticulum (ER)–mitochondria tether composed of four proteins, three of which contain a SMP (synaptotagmin-like mitochondrial-lipid binding protein) domain. No functional ortholog for any ERMES protein has been identified in metazoans. Here, we identified PDZD8 as an ER protein present at ER-mitochondria contacts. The SMP domain of PDZD8 is functionally orthologous to the SMP domain found in yeast Mmm1. PDZD8 was necessary for the formation of ER-mitochondria contacts in mammalian cells. In neurons, PDZD8 was required for calcium ion (Ca^{2+}) uptake by mitochondria after synaptically induced Ca^{2+}-release from ER and thereby regulated cytoplasmic Ca^{2+} dynamics. Thus, PDZD8 represents a critical ER-mitochondria tethering protein in metazoans. We suggest that ER-mitochondria coupling is involved in the regulation of dendritic Ca^{2+} dynamics in mammalian neurons.

Contacts between the endoplasmic reticulum (ER) and the mitochondria are thought to represent a signaling hub where Ca^{2+} and lipid exchange can occur between these two organelles (1, 2). In addition, changes in the extent of ER-mitochondria contacts have been reported in various models of neurodegenerative diseases such as Alzheimer's disease (3–5). Several proteins that are enriched at ER-mitochondria in mammalian cells, including Mitofusin2, have been proposed to play a role in modulating the contacts between these organelles (6–9). However, mutation of the genes encoding these proteins has complex and sometimes contradictory phenotypic consequences on ER-mitochondria contacts (10–12).

The ER–mitochondria encounter structure (ERMES) complex functions as a tether between the ER and mitochondria in budding yeast (1). Three out of four ERMES complex proteins (Mmm1, Mdm12, and Mdm34) contain an SMP domain. Trans-heterodimerization of SMP do-

mains within proteins such as extended synaptotagmin 2 (E-syt2) was recently proposed to participate in lipid exchange between ER and plasma membrane (13–15). Based on low levels of amino acid sequence homology, no ERMES complex ortholog has been identified in metazoans (16, 17) (fig. S1, C to E). Recent bioinformatics approaches predicted the existence of several SMP domain–containing proteins in metazoans (18, 19), including a protein of unknown function called PDZD8. A search of the PDB (Protein Data Bank) using the Phyre2 protein modeling server showed that the SMP-containing proteins E-syt2 (PDB code 4P42) and the ERMES complex protein Mdm12 (PDB code 5gyk), respectively, are similar to residues 92 to 367 and 105 to 287 of PDZD8 with >99.8% confidence [expected value of $<10^{-26}$ in hidden Markov models (HMM)-HMM–based lightning-fast iterative sequence search (HHBLITS)] (Fig. 1, B and C). Furthermore, there is a high correspondence in the secondary structure elements (SSEs) of the predicted SMP domain of PDZD8 and the actual SSEs in the SMP domains of E-syt2 and Mdm12 (Fig. 1D). These results strongly suggest that PDZD8 is an SMP-containing protein. We therefore explored the possibility that PDZD8 constitutes a structural and functional ortholog of the ERMES component Mmm1.

Investigating the functional similarity between the SMP domains of Mmm1 and PDZD8

Mmm1 and PDZD8 contain an N-terminal transmembrane domain followed by an SMP domain, although PDZD8 has a longer C-terminal extension, including predicted PDZ, C1, and coil-coiled (CC) domains (Fig. 1A). In addition, Mmm1 is the

only SMP-containing ERMES subunit localized to the ER in yeast (1, 20). Modeling indicated that the predicted SMP domains of PDZD8 and Mmm1 are structurally homologous with the SMP domains of E-syt2 and Mdm12 (Fig. 1, B and C, and fig. S1, A to C). To determine whether PDZD8 and Mmm1 are functionally homologous, we first expressed PDZD8 in yeast and tested its localization. PDZD8-Venus colocalized with yeast ER-resident protein Pho88, suggesting conserved and functional ER targeting of PDZD8 (fig. S2A).

Next, we investigated whether PDZD8 could functionally complement for Mmm1 function. Deletion of the *MMM1* gene resulted in critical cellular and mitochondrial defects, including (i) the collapse of the mitochondrial tubular network into one or two large spherical structures, (ii) severe mitochondrial inheritance defects during cell division, and (iii) the complete loss of mitochondrial DNA (mtDNA) (figs. S3 to S5) (21, 22). Because *mmm1Δ* cells rapidly accumulate suppressor mutations (23), we used a plasmid shuffling experimental strategy to replace endogenous *MMM1* with genes of interest to avoid adaptation to the loss of *MMM1* (fig. S3A). Briefly, we transformed a low-copy plasmid bearing genes of interest, including *PDZD8* variants under the *MMM1* promoter and a URA3 selectable marker (pRESC), into heterozygous *mmm1Δ*/*MMM1* diploid cells expressing mitochondria-targeted Cit1p-mCherry. Haploid cells containing the rescue plasmid and a deletion of *MMM1* (pRESC + *mmm1Δ*) were generated from the diploids and analyzed for functional rescue. Finally, to exclude the possibility of genomic adaptation, we tested whether the recovered phenotype could be reversed by loss of the rescue plasmid through 5-fluoroorotic acid (5-FOA) incubation, which is toxic to cells expressing URA3 and selects for spontaneous loss of pRESC (fig. S3A).

First, we attempted to rescue the *mmm1Δ* with the truncated form of PDZD8 containing the transmembrane and SMP domains (PDZD8^{TM-SMP}) or the SMP domain-swapped MMM1 with a PDZD8-SMP domain (*pMMM1-SMP$^{PDZD8\_full}$*) (fig. S3, B and C). However, these proteins were not able to restore the mitochondrial morphology, inheritance, and mtDNA maintenance defects, unlike wild-type *MMM1* (fig. S3, B and C).

Structural alignment of the SMP domains of Mmm1 and PDZD8 or Mdm12 revealed that the only major differences in SSEs reside within the two loops of the first β sheet (L1 and L2 for Pdzd8 and L1 for Mdm12) (fig. S1D). Thus, we next tested an MMM1 SMP-domain swap with PDZD8 that spared the original L1 and L2 MMM1-SMP regions (pMMM1-SMP$^{PDZD8+L1L2}$) (fig. S4). Surprisingly, expression of the yeast *MMM1*/mouse PDZD8 chimera containing L1 and L2 or MMM1/Mdm12 chimera containing L1 restored (i) retention of mtDNA in ~25% of cells examined (fig. S4, D and E), (ii) mitochondrial inheritance in ~50% of the cells examined (fig. S4, D and F), and (iii) normal tubular mitochondrial morphology in ~30% of the organelles examined (fig. S4, D and G; see fig. S5 for the development of the mitochondrial morphology quantification method).

[1]Department of Neuroscience, Columbia University Medical Center, Columbia University, New York, NY 10027, USA. [2]Mortimer B. Zuckerman Mind Brain Behavior Institute, Columbia University, New York, NY 10027, USA. [3]Kavli Institute for Brain Science, Columbia University, New York, NY 10027, USA. [4]Japan Science and Technology Agency (JST), Precursory Research for Embryonic Science and Technology (PRESTO), Tokyo, Japan. [5]Department of Pathology and Cell Biology, Columbia University, New York, NY 10032, USA. [6]Institute of Human Nutrition, Columbia University, New York, NY 10032, USA. [7]Simons Electron Microscopy Center, New York Structural Biology Center (NYSBC), New York, NY 10027, USA. [8]Center for Computational Biology and Bioinformatics, Department of Systems Biology, Columbia University, New York, NY 10032, USA. [9]Howard Hughes Medical Institute, Columbia University, New York, NY 10032, USA.
*These authors contributed equally to this work. †Corresponding author. Email: fp2304@cumc.columbia.edu
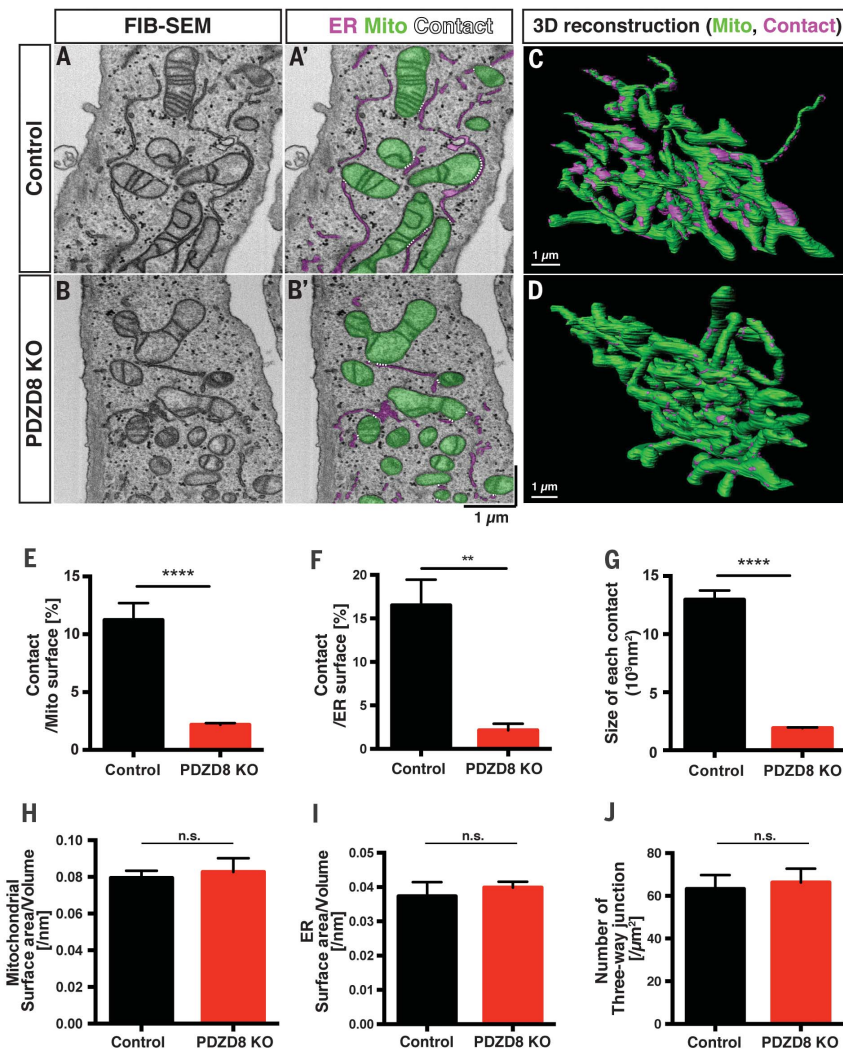
Fig. 1. The SMP domain–containing PDZD8 is a mammalian ortholog of yeast Mmm1 and is present at ER-mitochondria contact sites. (**A**) Domain organization of *S. cerevisiae* Mmm1 and mammalian PDZD8 proteins. (**B** and **C**) Superimposition of Phyre2 structural homology models for the SMP domains of PDZD8 over the crystal structures of mammalian E-syt2 (192 to 370 amino acids) (B) or *S. cerevisiae* Mdm12 (1 to 266 amino acids) (C). Root mean square deviation of atomic positions (RMSD) values show higher similarity with E-syt2 than Mdm12 (see fig. S1). (**D**) Predicted secondary structure of the SMP domain of PDZD8 (mouse) alignment with E-syt2 (human) and Mdm12 (*S. cerevisiae*) suggests a high degree of structural homology at the secondary structural level. Expected value = 3.5×10^{-26} (PDZD8 versus E-syt2). (**E**) Western blots of subcellular fractionation from HEK293T cells demonstrates the presence of endogenous PDZD8 in ER and MAM fractions. MAM fraction was isolated using a Percoll gradient and immunoblotted with antibodies to PDZD8, calnexin (for ER and MAM fractions), and cytochrome C (for mitochondrial fraction). (**F** to **K**) We

generated a mouse Neuro2a (N2a) cell line by knockin of Venus in the endogenous Pdzd8 genomic locus to create a C-terminal fusion PDZD8-Venus fusion protein by transfecting with a plasmid expressing guide RNA targeted to PDZD8 sequence and Cas9, together with the donor plasmid (see fig. S6A for details). N2a cells that had stably integrated the donor plasmid were enriched by selection with 600 µg/ml Geneticin (G418 sulfate). The targeted cells were transfected with a plasmid expressing Canx-mCherry (ER marker) and stained with antibodies to red fluorescent protein, GFP, and OXPHOS (oxidative phosphorylation) complex (mitochondrial marker). The stained cells were imaged with super-resolution microscopy (3D SIM). Images from a single plane [(F) to (I)] and a 3D reconstructed image (J) are shown. Arrowheads indicate the localization of PDZD8 at ER-mitochondria contact sites. (K) Analysis of colocalization between ER and PDZD8-Venus, and mitochondria and PDZD8-Venus using Mander's overlap demonstrates PDZD8 localization with ER but not mitochondria. Data are from four cells in each group. ***$P < 0.0005$, Student's *t* test.

Fig. 2. PDZD8 is required for the formation of the ER-mitochondria contacts in mammalian cells. (A to D) The 3D ultrastructural features of control HeLa cells or PDZD8-KO HeLa cells (24) were examined with FIB-SEM. [(A) and (B)] Representative individual electron micrographs of control (A and A′) or PDZD8-KO (B and B′) cells. The mitochondria and ER were labeled with green and magenta, respectively (A′ and B′). The ER-mitochondria contact sites are indicated by dashed white lines (<25 nm distance between membranes). [(C) and (D)] The 3D distribution of single continuous mitochondria (green) and corresponding ER-mitochondria contact sites (magenta) reconstructed from FIB-SEM image stacks of a control (A) and a PDZD8-KO HeLa cell (B). (E to J) Quantification of the ER-mitochondria contact sites [(E) to (G)], mitochondrial (H), and ER [(I) and (J)] morphology from the 3D reconstructions. (E) Percentage of mitochondrial surface area in direct contact with ER is significantly decreased in PDZD8-KO HeLa cells compared with control HeLa cells (see also movies S2 to S5). (F) Percentage of ER surface area in contact with mitochondria is also significantly reduced in PDZD8-KO HeLa cells compared with control HeLa cells. (G) Average surface area of ER-mitochondria contact sites in PDZD8-KO HeLa cells is significantly decreased compared with control cells. [(H) and (I)] Mitochondrial (H) or ER (I) surface area to volume ratio is not significantly different between control and PDZD8-KO cells, suggesting the absence of significant change in the overall structure of both organelles. (J) Quantification of the number of three-way junctions in the ER network, a quantitative index of the extent of tubular ER (25, 26). The number of three-way junctions in the ER structure is not significantly different in PDZD8-KO HeLa cells compared with control cells. [(E), (G), and (H)] The total number of the contact sites identified in these serial EM reconstructions was 2011 (control) and 3197 (PDZD8-KO) from 10 control and 11 PDZD8-KO mitochondria fully reconstructed. For (F), (I), and (J), the ER network was quantified in regions surrounding mitochondria in four to six cells of each genotype. A nonparametric Mann-Whitney test was used to test statistical significance. **P < 0.01; ****P < 0.0001. Cells quantified are from two independent cell cultures. Data are displayed as mean ± standard error of the mean. n.s., not significant.

Plasmid loss by 5-FOA reversed the rescue phenotype (fig. S4).

Despite containing the original L1 and L2 loops from MMM1, the SMP domain of the rescue construct (pMMM1-SMP$^{PDZD8+L1L2}$) consisted of >75% of the primary sequence found in PDZD8, with only ~15% sequence identity to MMM1. Moreover, although the rescue with pMMM1-SMP$^{PDZD8+L1L2}$ was partial, it was similar to that observed when the SMP domain of Mmm1 was replaced with the SMP domain of another ERMES protein, Mdm12 (fig. S4). Thus, the SMP domain of metazoan PDZD8 is as functional as a yeast SMP domain.

Thus, SMP domains from yeast MMM1 represent a structural and functional ortholog of the SMP domain of metazoans PDZD8. Additionally, we find that functional homology between MMM1 and PDZD8 SMP domains does not extend to the L1 and L2 loops. The L1 and L2 loops are poorly conserved even among the Ascomycota, such as *Schizosaccharomyces pombe*, *Magnaporthe oryzae*, and *Neurospora crassa*. Thus, variability in the L1 and L2 loops may lend specificity of SMP domains to a particular functional context in different organisms.

PDZD8 is an ER protein localized at ER-mitochondria contact sites

Because both Mmm1 and PDZD8 reside in the ER in *Saccharomyces cerevisiae*, we examined the subcellular localization of PDZD8 in mammalian cells. PDZD8-HA in HeLa cells showed extensive colocalization with ER-targeted Calnexin–yellow fluorescent protein (fig. S2B). To examine the localization of endogenous PDZD8, we produced a PDZD8-Venus knockin Neuro2a (N2a) cell line in which Venus fluorescent protein was knocked into the PDZD8 genomic locus using CRISPR-Cas9 (fig. S6A). The endogenous expression was confirmed by immunofluorescence (Fig. 1, F to K) and Western blots using antibodies to PDZD8 and green fluorescent protein (GFP) (fig. S6, B and C). ER and mitochondria in PDZD8-Venus knockin N2a (N2a$^{PDZD8-Venus}$) cells were labeled by coexpression of Calnexin-mCherry and staining with an antibody cocktail against mitochondrial proteins (OXPHOS). Super-resolution imaging with structured illumination microscopy (SIM) revealed that endogenous PDZD8-Venus was localized in the ER and also found at ER-mitochondria contact sites (Fig. 1, F to K; fig. S6, E to H; and movie S1).

Subcellular fractionation of human embryonic kidney (HEK) 293T cells using antibody to PDZD8 (24) and N2a$^{PDZD8-Venus}$ cells confirmed that PDZD8 was enriched in the ER and present at the mitochondria-associated endoplasmic reticulum membrane (MAM) fraction but not detected in the pure mitochondrial fraction (Fig. 1E and fig. S6D). Thus PDZD8 is an ER-resident protein that is also localized at ER-mitochondria contact sites.

PDZD8 is required for formation of ER-mitochondria membrane contacts

Because PDZD8 was present at ER-mitochondria contact sites and contained an SMP domain

structurally and functionally orthologous to yeast ERMES complex protein Mmm1, we investigated whether PDZD8 functioned as a tethering protein and whether it was required for the formation of ER-mitochondria contacts. To map ER-mitochondria contacts quantitatively, we performed three-dimensional serial scanning electron microscopy (3D SEM) using focus ion beam–scanning EM (FIB-SEM) (Fig. 2 and movies S2 to S5). The 3D reconstructions of FIB-SEM stacks showed that the volume-surface ratio of mitochondria (Fig. 2H) and ER (Fig. 2I) and the number of three-way junctions (an index often used to measure ER tubule complexity (25, 26) (Fig. 2J) were not significantly different between the control and PDZD8 knockout (KO) cells (24). Thus, deletion of PDZD8 had no detectable effect on the structure of mitochondria and ER networks (Fig. 2, H to J, and movies S2 to S5).

We also quantified the size and distribution of ER-mitochondria contact sites [defined as membrane appositions between the two organelles with less than 25 nm distance (16)] on 10 mitochondrial segments from five HeLa cells (total surface area 2.8×10^2 µm^2; total volume 13 µm^3) and 11 mitochondrial segments from six PDZD8 KO HeLa cells (total surface area 3.0×10^2 µm^2; total volume 17 µm^3). As previously reported (2, 27, 28), 11.2% of the mitochondrial surface area was in contact with ER in control HeLa cells but, strikingly, only 2.2% of mitochondrial surface was in contact with ER in PDZD8 KO cells (Fig. 2E). We also normalized the surface of ER-mitochondria contacts relative to ER surface area: 16.5% of the ER surface area was in contact with the mitochondria in control cells, but only 2.1% of ER surface was in contact with the mitochondria in PDZD8 KO cells (Fig. 2F). Furthermore, the average surface of individual ER-mitochondria contacts was also decreased by ~80% in PDZD8 KO HeLa compared with control HeLa cells (Fig. 2G). These results strongly suggested that PDZD8 is required for tethering ER and mitochondria membranes in human cells.

PDZD8-mediated tethering is critical for ER-mitochondria Ca^{2+} transfer

ER-mitochondria contacts are emerging as signaling hubs and have been proposed to play a critical role in Ca^{2+} exchange between these two organelles (2, 28–30). Upon activation of ryanodine and/or inositol-1,4,5-trisphosphate (IP$_3$) receptors (IP$_3$R), Ca^{2+} released from the ER transiently reaches concentrations high enough to open the mitochondrial calcium uniporter (MCU) complex at the ER-mitochondria contacts (30–32), promoting efficient mitochondrial Ca^{2+} uptake. To determine whether ER-mitochondria tethering by PDZD8 plays a role in Ca^{2+} transfer between these two organelles, we monitored Ca^{2+} dynamics in the ER and mitochondria simultaneously (33). We expressed genetically encoded Ca^{2+} indicators (GECI) targeted to the ER (red fluorescence; R-CEPIA1er) (33) and the mitochondria (green fluorescence; CEPIA3mt) (33). In control NIH3T3 cells, stimulation of purinergic recep-
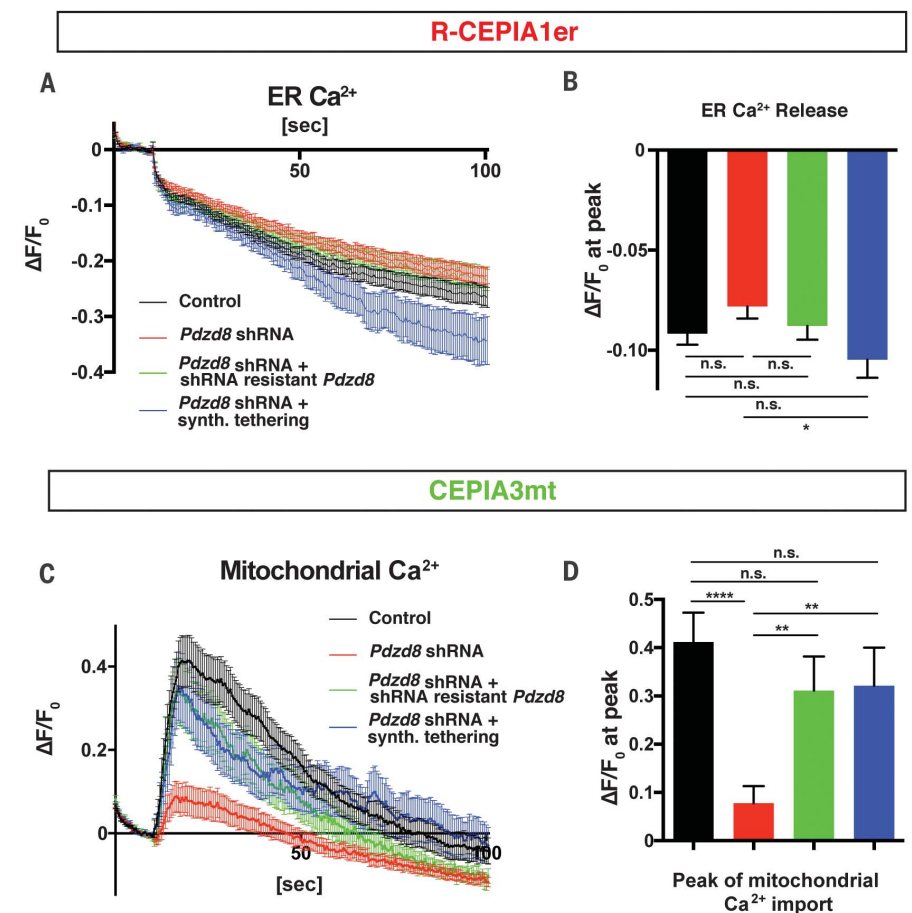
tors with extracellular adenosine 5′-triphosphate (ATP) (34), which generates IP$_3$, robustly activates IP$_3$R and induced Ca^{2+} release from ER stores leading to rapid Ca^{2+} import into mitochondria (Fig. 3 and movie S6). In contrast, in NIH3T3 cells expressing short hairpin RNA (shRNA) efficiently knocking down Pdzd8 (fig. S6, B and C, and fig. S7, B and C), Ca^{2+} import into mitochondria after ATP stimulation was significantly reduced, even though Ca^{2+} release from the ER was not significantly affected (Fig. 3; movie S7; and fig. S8, C and D). In addition, expression of an shRNA-resistant Pdzd8 cDNA restored Ca^{2+} uptake into mitochondria in ATP-treated NIH3T3 cells expressing Pdzd8 shRNA (Fig. 3). Importantly, resting Ca^{2+} levels in both ER and mitochondria

(fig. S8, E and F), ER-independent mitochondrial Ca^{2+} import (fig. S9, A and B), and mitochondrial membrane potential (fig. S9, C and D) were not significantly altered in PDZD8-deficient cells. Furthermore, expression levels of mitochondrial Ca^{2+} regulatory proteins and other tethering proteins were not altered in Pdzd8 knockdown NIH3T3 cells (fig. S9, E to H).

To determine whether this reduced mitochondrial Ca^{2+} import in Pdzd8-deficient cells was indeed due to the loss of the ER-mitochondria contacts, we performed a rescue experiment using a synthetic tethering protein (28) that restored ER-mitochondria contacts (fig. S8A). Expression of a synthetic ER-mitochondria tethering construct almost completely rescued the mitochondrial

Fig. 3. PDZD8-dependent membrane contacts are required for ER-mitochondria Ca^{2+} transfer. NIH3T3 cells were transfected with plasmids encoding mitochondria-targeted GECI (CEPIA3mt), ER-targeted GECI (R-CEPIA1er), and combinations of constructs indicated [a control plasmid (Control), a Pdzd8 shRNA plasmid, a Pdzd8 shRNA-resistant Pdzd8 cDNA-expressing plasmid, or a synthetic ER-mitochondria tethering protein]. Cells were stimulated with 200 µM extracellular ATP, and fluorescence from CEPIA3mt and R-CEPIA1er was measured. (A to D) Changes of fluorescence (ΔF) from R-CEPIA1er [(A) and (B)] or CEPIA3mt [(C) and (D)], normalized by basal signals before the stimulation (F$_0$). Peak intensity of ΔF/F$_0$ at 10 s after ATP stimulation shows significant reduction of mitochondrial Ca^{2+} uptake [(C) and (D)], but not ER Ca^{2+} release [(A) and (B)], in Pdzd8-depleted cells (red lines and bars) compared with those in the control (black lines and bars). This altered phenotype is rescued by introducing a shRNA-resistant Pdzd8 plasmid (green lines and bars) or a synthetic ER-mitochondria tethering protein (blue lines and bars). n = 67 for control, 71 for Pdzd8-KD, 32 for Pdzd8 rescue, and 30 for tethering. Statistical significance: n.s., P > 0.05; *P < 0.05; **P < 0.01; ****P < 0.0001, according to unpaired t test with Welch's correction.
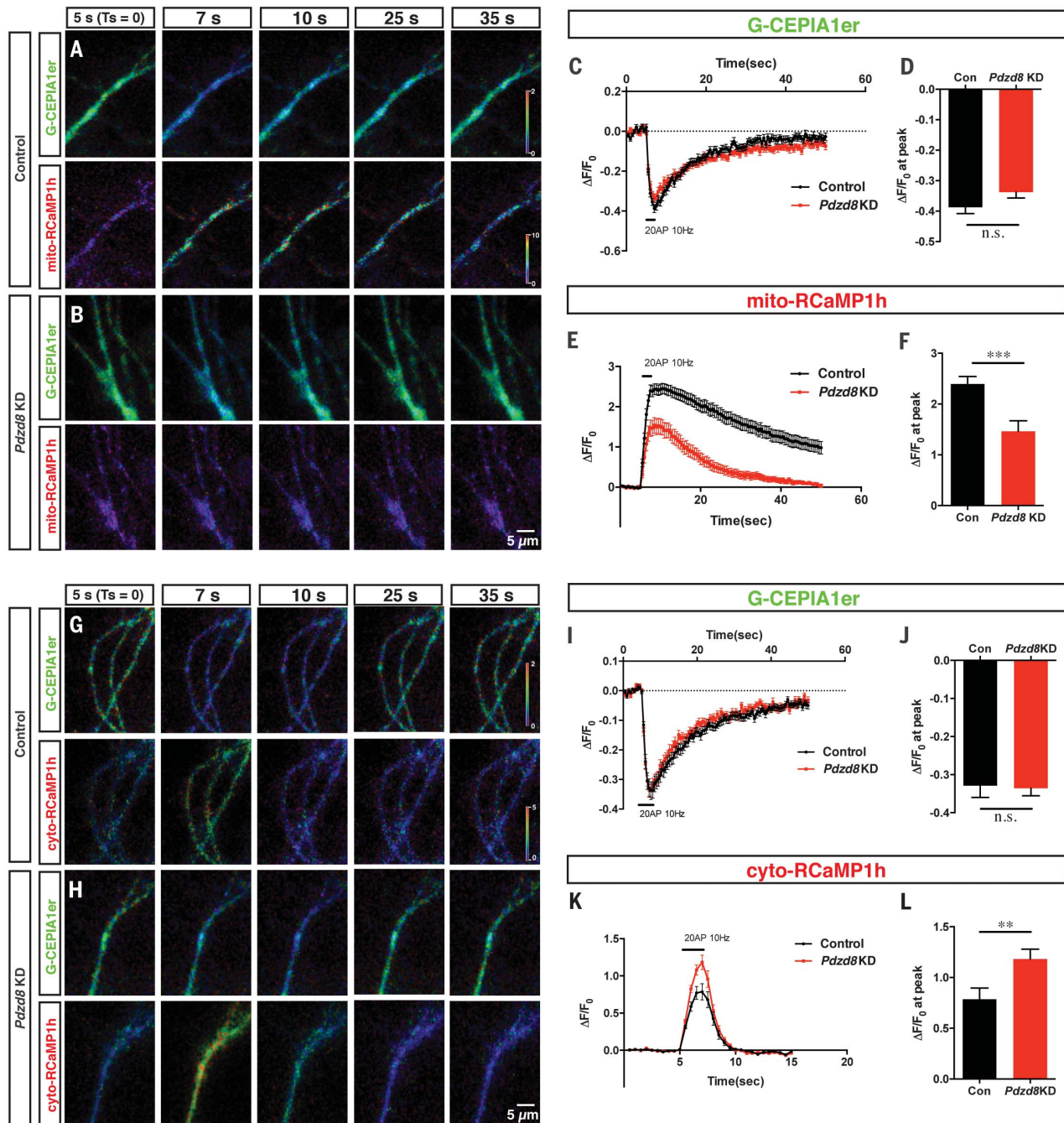
Fig. 4. PDZD8 loss of function in cortical neurons identifies a novel role for ER-mitochondria interface in the regulation of cytoplasmic Ca²⁺ dynamics in dendrites. (**A** to **F**) Dendritic ER and mitochondrial Ca²⁺ dynamics were monitored using G-CEPIA1er and mito-RCaMP1h, respectively. G-CEPIA1er and mito-RCaMP1h were cotransfected with control or *Pdzd8* shRNA plasmids using ex utero electroporation at embryonic day 15.5 and imaged at 19 to 22 days in vitro (DIV). Proximal dendrites of cortical pyramidal neurons display significant ER Ca²⁺ release and mitochondrial Ca²⁺ uptake after physiological stimulation of presynaptic release (20 AP at 10 Hz). Representative images are displayed as normalized ratio (ΔF/F₀) of each probe [(A) and (B)]. This stimulation evokes normal ER Ca²⁺ release in dendrites of both control and PDZD8-deficient neurons [(C) and (D)] but shows

significantly decreased mitochondrial Ca²⁺ import [(E) and (F)]. $n = 63$ dendritic segments from 18 neurons for control and 28 dendritic segments from 14 neurons for *Pdzd8* knockdown. (**G** to **L**) Dendritic ER (G-CEPIA1er) and cytosolic Ca²⁺ (RCaMP1h) levels were visualized before and after 20 AP in 21 to 22 DIV cortical neurons. [(G) and (H)] Cropped images show fluorescence as ratio normalized by basal signals before stimulation (ΔF/F₀). Cytosolic Ca²⁺ accumulation is significantly higher in *Pdzd8* knockdown neurons compared with control [(K) and (L)] despite unchanged ER Ca²⁺ release evoked by synaptic stimulation [(I) to (J)]. $n = 30$ dendritic segments from 10 neurons for control and 39 dendritic segments from 13 neurons for *Pdzd8* knockdown. Statistical significance: n.s., $P > 0.05$; **$P < 0.01$; ***$P < 0.001$, according to unpaired t test with Welch's correction.
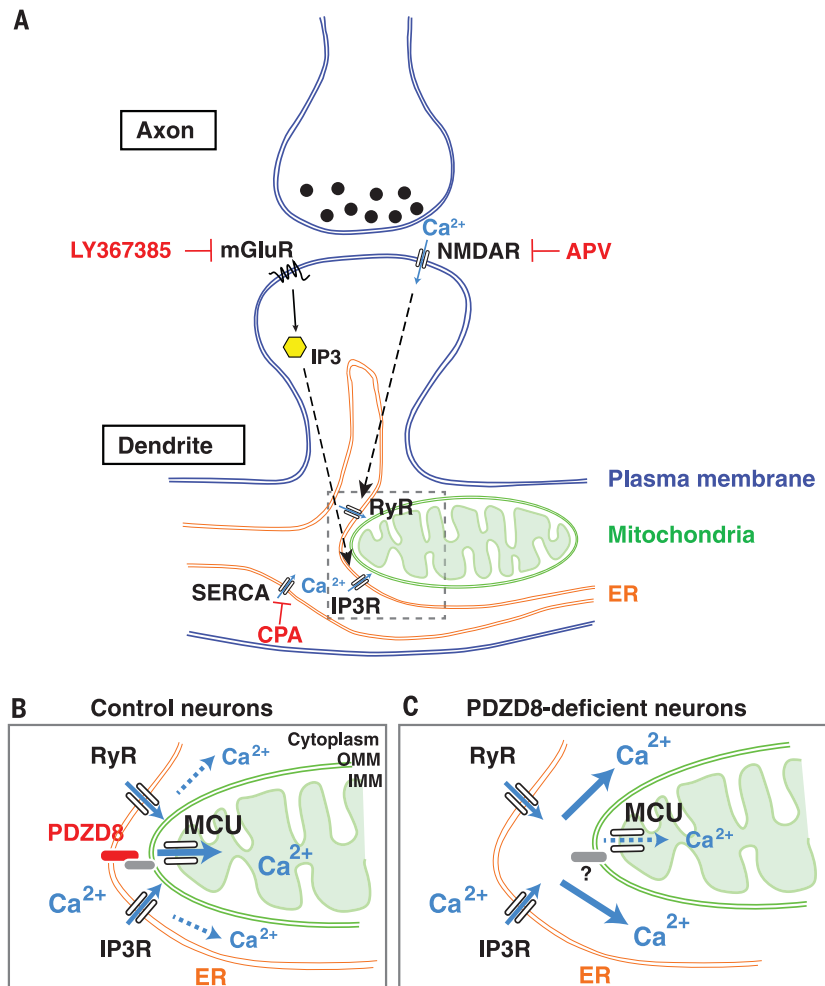
Fig. 5. PDZD8 is an ER-mitochondria tethering protein regulating dendritic Ca^{2+} dynamics in neurons. Schema summarizing the main findings in this study. (**A**) In dendrites of cortical pyramidal neurons, synaptically induced ER Ca^{2+} release requires both mGluR and NMDA receptor (see results in fig. S12). Our results demonstrate that the majority of synaptically induced Ca^{2+} imported into dendritic mitochondria originates from ER stores. (**B** and **C**) Our results also demonstrate that in neuronal dendrites, PDZD8-dependent ER-mitochondria tethering plays a critical role in cytoplasmic Ca^{2+} homeostasis because in the absence of PDZD8 (C), a significantly higher fraction of synaptically induced Ca^{2+} release from the ER ends up in the cytoplasm rather than in the mitochondrial matrix, compared with control (B).

Ca^{2+} uptake induced by ATP application in PDZD8-deficient cells back to control levels (Fig. 3). Thus, our results demonstrate that ER-mitochondria tethering mediated by PDZD8 is required for efficient Ca^{2+} transfer from ER into mitochondria in metazoan cells.

Synaptically induced Ca^{2+} release from ER stores triggers mitochondrial Ca^{2+} uptake

Cytoplasmic Ca^{2+} dynamics in dendrites of neurons are critical for physiological responses, including synaptic integration and plasticity (35, 36). Although several studies have suggested that ER stores and mitochondria can influence dendritic Ca^{2+} dynamics (37–47), the functional importance of ER-mitochondria contacts is unknown in neurons. PDZD8 was expressed at high levels throughout the developing and adult mouse central nervous system (CNS), including in the neocortex (fig. S10). Thus, we investigated whether ER-mitochondria tethering by PDZD8 affected Ca^{2+} dynamics in dendrites of mouse cortical pyramidal neurons.

We used green (G)–CEPIA1er and mitochondria-targeted RCaMP1h (mito-RCaMP1h) to visualize ER ([Ca^{2+}]$_{ER}$) and mitochondrial matrix Ca^{2+} ([Ca^{2+}]$_{mito}$) dynamics simultaneously (33, 48) in synaptically mature cortical pyramidal neurons. We induced synaptic activity by stimulation with a concentric bipolar electrode [20 action potentials (AP) at 10Hz], which efficiently triggers presynaptic release in close proximity to the dendrites of target neurons (49). The dendrites of untreated, control cortical pyramidal neurons showed robust ER Ca^{2+} release and mitochondrial Ca^{2+} uptake after synaptic stimulation (fig. S12). Mitochondrial Ca^{2+} import in dendrites was dependent on ER Ca^{2+} release by applying a sarco/endoplasmic

reticulum Ca^{2+}-ATPase (SERCA) inhibitor as shown by application of cyclopiazonic acid (CPA). CPA treatment efficiently depleted [Ca^{2+}]$_{ER}$ and also abolished mitochondrial Ca^{2+} uptake (fig. S12, A to F). Thus, Ca^{2+} released from ER stores is the main source of mitochondrial Ca^{2+} import in dendrites of cortical pyramidal neurons. Previous studies have suggested that activation of postsynaptic *N*-methyl-D-aspartate (NMDA) receptors and/or metabotropic glutamate receptors (mGluR) trigger efficient Ca^{2+} release from ER stores (40, 41, 44–46, 50). Consistent with this, incubation with the NMDA receptor antagonist D-2-amino-5-phosphonovaleric acid or the mGluR1 blocker LY367385 abolished ER Ca^{2+} release and suppressed mitochondrial Ca^{2+} import (fig. S12, G to N). Thus, as expected, activation of both NMDA receptor and mGluR1 are required for synaptically evoked Ca^{2+} release from ER stores in the dendrites of cortical pyramidal neurons (Fig. 5A).

PDZD8 regulates dendritic Ca^{2+} dynamics in cortical neurons

Pdzd8 knockdown in cortical layer II/III pyramidal neurons did not impair the overall structure and distribution of dendritic ER and mitochondria in vivo (fig. S11). To determine whether PDZD8-dependent ER-mitochondria membrane tethering regulates ER and mitochondrial Ca^{2+} dynamics in neuronal dendrites, we introduced G-CEPIA1er and mito-RCaMP1h with either control or *Pdzd8* shRNA using ex utero electroporation in cortical pyramidal neurons. After physiological synaptic stimulation (20 AP at 10 Hz), Ca^{2+} release from ER stores was coupled with robust mitochondrial Ca^{2+} import in dendrites expressing control shRNA (Fig. 4, A to F, and movie S8). However, mitochondrial Ca^{2+} import was significantly reduced in *Pdzd8* knockdown neurons, consistent with data obtained in NIH3T3 cells (Fig. 4, B, E, and F, and movie S9). Expression levels of MCU or proteins proposed to regulate ER-mitochondria contacts (PIPIP51 and VDAC1) were not changed in *Pdzd8* knockdown neurons (fig. S13, A to D). Furthermore, mitochondrial Ca^{2+} import and extrusion kinetics, as well as resting Ca^{2+} amount in ER and mitochondria, were not altered in PDZD8-deficient neurons (fig. S13, E to J). These results strongly suggest that the significant reduction of mitochondrial Ca^{2+} import upon induction of ER Ca^{2+} release in dendrite PDZD8-deficient neurons is most likely due to the loss of ER-mitochondria contacts rather than to secondary effects due to alteration of the mitochondrial Ca^{2+} import machinery.

Finally, we investigated whether this uncoupling of ER-mitochondria Ca^{2+} exchange by PDZD8 loss of function resulted in impaired cytosolic Ca^{2+} ([Ca^{2+}]$_c$) dynamics. To do this, we coelectroporated G-CEPIA1er and cytosolic RCaMP1h together with control or *Pdzd8* shRNA and imaged them before and after synaptic stimulation (20 AP at 10 Hz). [Ca^{2+}]$_c$ levels were significantly elevated in *Pdzd8* knockdown dendrites compared with control dendrites (Fig. 4, G to L). Thus, a significant fraction of Ca^{2+} released from ER stores is directly imported

into mitochondria upon synaptic activation in control dendrites, and PDZD8 regulates cytoplasmic Ca^{2+} dynamics in dendrites through its function in ER-mitochondria tethering.

Here, we have identified PDZD8 as an ER-mitochondria tethering protein in metazoan cells and demonstrated that the SMP domain–containing protein PDZD8 might represent a structural and functional ortholog of the yeast ERMES protein component Mmm1. Furthermore, our results also demonstrate the importance of ER-mitochondria tethering for dendritic Ca^{2+} homeostasis in mammalian neurons (Fig. 5, B and C). Dendritic Ca^{2+} dynamics play several critical functions ranging from synaptic integration properties to various forms of synaptic plasticity (35, 36). Cytoplasmic Ca^{2+} microdomains in neuronal dendrites represent a cellular mechanism recently proposed to regulate branch-specific synaptic integration and plasticity (51, 52). We suggest that the control of cytoplasmic Ca^{2+} dynamics in dendrites involves ER-mitochondria coupling and, by analogy to its proposed functions in non-neuronal cells, this organelle interface might play other important biological functions such as lipid exchange and coupling of mitochondrial DNA replication with mitochondrial fission in neurons.

REFERENCES AND NOTES

1. B. Kornmann et al., Science 325, 477–481 (2009).
2. R. Rizzuto et al., Science 280, 1763–1766 (1998).
3. E. Area-Gomez et al., Am. J. Pathol. 175, 1810–1816 (2009).
4. E. Area-Gomez, E. A. Schon, Curr. Opin. Genet. Dev. 38, 90–96 (2016).
5. S. Paillusson et al., Trends Neurosci. 39, 146–157 (2016).
6. O. M. de Brito, L. Scorrano, Nature 456, 605–610 (2008).
7. G. Szabadkai et al., J. Cell Biol. 175, 901–911 (2006).
8. K. J. De Vos et al., Hum. Mol. Genet. 21, 1299–1311 (2012).
9. Y. Lim, I. T. Cho, L. J. Schoel, G. Cho, J. A. Golden, Ann. Neurol. 78, 679–696 (2015).
10. P. Cosson, A. Marchetti, M. Ravazzola, L. Orci, PLOS ONE 7, e46293 (2012).
11. R. Filadi et al., Proc. Natl. Acad. Sci. U.S.A. 112, E2174–E2181 (2015).
12. D. Naon et al., Proc. Natl. Acad. Sci. U.S.A. 113, 11249–11254 (2016).
13. A. P. AhYoung et al., Proc. Natl. Acad. Sci. U.S.A. 112, E3179–E3188 (2015).
14. C. M. Schauder et al., Nature 510, 552–555 (2014).
15. H. Jeong, J. Park, C. Lee, EMBO Rep. 17, 1857–1871 (2016).
16. S. C. Helle et al., Biochim. Biophys. Acta 1833, 2526–2541 (2013).
17. V. Alva, A. N. Lupas, Biochim. Biophys. Acta 1861, 913–923 (2016).
18. K. O. Kopec, V. Alva, A. N. Lupas, Bioinformatics 26, 1927–1931 (2010).
19. I. Lee, W. Hong, FASEB J. 20, 202–206 (2006).
20. B. Kornmann, P. Walter, J. Cell Sci. 123, 1389–1393 (2010).
21. T. Hanekamp et al., Genetics 162, 1147–1156 (2002).
22. A. E. Hobbs, M. Srinivasan, J. M. McCaffery, R. E. Jensen, J. Cell Biol. 152, 401–410 (2001).
23. A. B. Lang, A. T. John Peter, P. Walter, B. Kornmann, J. Cell Biol. 210, 883–890 (2015).
24. S. Zhang, J. Sodroski, Virology 481, 73–78 (2015).
25. L. M. Westrate, J. E. Lee, W. A. Prinz, G. K. Voeltz, Annu. Rev. Biochem. 84, 791–811 (2015).
26. S. Chen et al., Proc. Natl. Acad. Sci. U.S.A. 112, 418–423 (2015).
27. R. Stoica et al., Nat. Commun. 5, 3996 (2014).
28. G. Csordás et al., J. Cell Biol. 174, 915–921 (2006).
29. A. A. Rowland, G. K. Voeltz, Nat. Rev. Mol. Cell Biol. 13, 607–625 (2012).
30. M. Giacomello et al., Mol. Cell 38, 280–290 (2010).
31. G. Csordás et al., Mol. Cell 39, 121–132 (2010).
32. M. Patron et al., Mol. Cell 53, 726–737 (2014).
33. J. Suzuki et al., Nat. Commun. 5, 4153 (2014).
34. G. Burnstock, Cell. Mol. Life Sci. 64, 1471–1483 (2007).
35. N. Spruston, Nat. Rev. Neurosci. 9, 206–221 (2008).
36. P. J. Sjöström, E. A. Rancz, A. Roth, M. Häusser, Physiol. Rev. 88, 769–840 (2008).
37. S. H. Lee et al., J. Neurosci. 32, 5953–5963 (2012).
38. S. A. Thayer, R. J. Miller, J. Physiol. 425, 85–115 (1990).
39. S. J. Cherra 3rd, E. Steer, A. M. Gusdon, K. Kiselyov, C. T. Chu, Am. J. Pathol. 182, 474–484 (2013).
40. M. F. Yeckel, A. Kapur, D. Johnston, Nat. Neurosci. 2, 625–633 (1999).
41. N. Emptage, T. V. Bliss, A. Fine, Neuron 22, 115–124 (1999).
42. M. Nishiyama, K. Hong, K. Mikoshiba, M. M. Poo, K. Kato, Nature 408, 584–588 (2000).
43. E. A. Finch, G. J. Augustine, Nature 396, 753–756 (1998).
44. H. Takechi, J. Eilers, A. Konnerth, Nature 396, 757–760 (1998).
45. S. S. Wang, W. Denk, M. Häusser, Nat. Neurosci. 3, 1266–1273 (2000).
46. M. Miyata et al., Neuron 28, 233–244 (2000).
47. K. F. Lee, C. Soares, J. P. Thivierge, J. C. Béïque, Neuron 89, 784–799 (2016).
48. J. Akerboom et al., Front. Mol. Neurosci. 6, 2 (2013).
49. A. Maximov, Z. P. Pang, D. G. Tervo, T. C. Südhof, J. Neurosci. Methods 161, 75–87 (2007).
50. A. Verkhratsky, Physiol. Rev. 85, 201–279 (2005).
51. A. Losonczy, J. K. Makara, J. C. Magee, Nature 452, 436–441 (2008).
52. M. E. Sheffield, D. A. Dombeck, Nature 517, 200–204 (2015).

Science

ER-mitochondria tethering by PDZD8 regulates Ca^{2+} dynamics in mammalian neurons

Yusuke Hirabayashi, Seok-Kyu Kwon, Hunki Paek, Wolfgang M. Pernice, Maëla A. Paul, Jinoh Lee, Parsa Erfani, Ashleigh Raczkowski, Donald S. Petrey, Liza A. Pon and Franck Polleux

Making the right contacts

Contacts between the endoplasmic reticulum (ER) and mitochondria mediate key physiological processes such as Ca^{2+} exchange and lipid biogenesis. In yeast, ER and mitochondria are tethered by a complex of four proteins called ERMES. However, no functional orthologs of these ERMES complex proteins have been identified in metazoans. Hirabayashi *et al.* identified PDZD8 as a structural and functional ortholog of the yeast ERMES protein MMM1 (see the Perspective by Lombardi and Elrod). PDZD8 was found at ER-mitochondria contact sites and was required for ER-mitochondria tethering in mammalian cells. In neuronal dendrites, PDZD8 regulated synaptically evoked Ca^{2+} dynamics, which underscores the importance of interorganelle membrane contacts in cell physiology.

Science, this issue p. 623; see also p. 591

ARTICLE TOOLS	http://science.sciencemag.org/content/358/6363/623
SUPPLEMENTARY MATERIALS	http://science.sciencemag.org/content/suppl/2017/11/02/358.6363.623.DC1
RELATED CONTENT	http://science.sciencemag.org/content/sci/358/6363/591.full
REFERENCES	This article cites 64 articles, 18 of which you can access for free http://science.sciencemag.org/content/358/6363/623#BIBL
PERMISSIONS	http://www.sciencemag.org/help/reprints-and-permissions

Use of this article is subject to the Terms of Service

Supplementary Materials for

ER-mitochondria tethering by PDZD8 regulates Ca²⁺ dynamics in mammalian neurons

Yusuke Hirabayashi,* Seok-Kyu Kwon,* Hunki Paek, Wolfgang M. Pernice,
Maëla A. Paul, Jinoh Lee, Parsa Erfani, Ashleigh Raczkowski,
Donald S. Petrey, Liza A. Pon, Franck Polleux[†]

*These authors contributed equally to this work.
[†]Corresponding author. Email: fp2304@cumc.columbia.edu

This PDF file includes:

Materials and Methods
Figs. S1 to S13
References

Other Supplementary Material for this manuscript includes the following:
(available at www.sciencemag.org/cgi/content/full/358/6363/623/DC1)

Movies S1 to S9

Material and Methods
Animals
All animals were housed and handled according to protocols approved by the Institutional Animal Care and Use Committee (IACUC) at Columbia University. Time-pregnant CD1 females were purchased from Charles River (Wilmington MA, USA).

Constructs
pCAG::mito (CoxVIII)-mTAGBFP2 was previously described (*53*). C-terminal HA-tagged mouse PDZD8 was cloned with from cDNA library obtained from C57/Bl6 mouse brain by PCR. pCAG PDZD8HA was created by inserting the mouse PDZD8 coding sequence at XhoI-NotI sites of pCIG2 vector. pCAG PDZD8HA resistant to shPDZD8 was created by primers having silent mutations at the shPDZD8 targeting site. pLKO1.5 shPDZD8 (TRCN0000431056) was from Sigma Aldrich. Control vector used in shRNA experiments is the pLKO1 vector from TRC library (expressing small RNA sequence CCGCAGGTATGCACGCGT). pCAG::Calnexin-YFP was created by replacing mitochondria targeting sequence of pCAG::mito-YFP (*53*) with Calnexin coding sequence. pCAG::Calnexin-mCherry was created by replacing YFP sequence with mCherry sequence. Synthetic ER-mitochondria tethering construct was created by replacing mitochondria targeting sequence of pCAG-mito-mtagBFP2 (*53*) with DNA oligomers coding a mitochondria targeting sequence (AKAP) and inserting DNA oligomers coding ER targeting sequence (UBC6) at the 3' end of mtagBFP2 at the BsrGI site (*28*). pCMV::CEPIA3mt, pCMV::R-CEPIA1er, and pCMV::G-CEPIA1er were gifts from Masamitsu Iino (Addgene plasmid # 58219, 58216, 58215, respectively). For cytosolic RCaMP1h, we inserted RCaMP1h from pRSET-RCaMP1h (Addgene plasmid #42874) to pCIG2 by replacing IRES-GFP. pCAG::mito-RCaMPh1 was generated by swapping GCaMP5G with RCaMP1h in pCAG::mito-GCaMP5G (*54*). pCAG::G-CEPIA1er and pCAG::CEPIA3mt were created by inserting G-CEPIA1er and CEPIA3mt into pCAG vector, respectively.

Generation of Pdzd8-Venus knock-in Neuro2a cell line
For CRISPR-Cas9 plasmid, CRISPR guide RNA was designed using Optimized CRISPR Design tool (http://crispr.mit.edu) and cloned into pSpCas9(BB)-2A-Puro (PX459) V2.0 (a gift from Feng Zhang; Addgene plasmid # 62988) as previously described (*55*). For the donor vector, 5' arm sequence was amplified from pCAG-PDZD8HA with primers containing silent mutations at the CRISPR target site. 3'UTR sequence was cloned from a bacterial artificial chromosome (RP23-373G10, BACPAC resources). These sequences, together with Venus, P2A, and Neo sequences, were cloned into the XhoI-NotI restriction enzyme sites of pCIG2 with In-Fusion HD cloning kit (Takara Bio). Neuro2a cells were transfected with CRISPR-Cas9 plasmid and the donor vector by Jetprime (Polyplus-transfection). Cells were replated after 24 hours and treated with puromycin (2μg/ml) to select transfected cells for 2 days. The selected cells were then cultured with Geneticin (G418 sulfate, 400 μg/ml; Sigma-Aldrich A-1720) to select successfully recombined cells.

Super-resolution imaging (3D-SIM)
Neuro2a-PDZD8-Venus-KI cells were plated on a High-performance cover glass (D =

0.17, Carl Zeiss Microscopy) and transfected with pCAG Canx-mCherry by Jetprime and cultured for two days. Transfected cells were fixed with 4% PFA for 10' followed by fixation with ice cold methanol for 6min. Cells were then treated with 3% BSA/PBS for 30' followed by an incubation with primary antibodies against GFP (1:2000, GFP-1020; Aves labs), RFP (1:1000, ab62341; Abcam), and anti-OxPhos Complex (1:500, Thermo Fisher Scientific) overnight at 4ºC. After treated with secondary antibodies anti-mouse IgG Alexa 405, anti-chicken IgG Alexa 488, and anti-rabbit IgG Alexa 546 (Thermo Fisher Scientific), the coverslip was mounted on a slide glass with ProLong® Diamond Antifade Mountant (Thermo Fisher Scientific). Cells were imaged with Nikon Ti Eclipse inverted microscope equipped with a SIM illuminator, an iXon Ultra 897 camera (Andor), and a × 100 plan apochromat immersion oil objective (NA 1.49). Image reconstruction and analysis were performed with the NIS-Elements software (Nikon).

Cell Culture
Neuro2a (ATCC), HeLa cells (ATCC), PDZD8 KO HeLa cells (gift from Dr. Joseph Sodroski) and NIH3T3 cells (ATCC) were maintained with Dulbecco's Modified Eagle Medium (Thermo Fisher Scientific) supplemented with 10% FBS (Gemini Bio-products) and 1% Penicillin-Streptomycin (Thermo Fisher Scientific) under 5% CO_2.

Neuronal Culture
Embyonic mouse cortices (E15.5) were *ex utero* electroporated following the injection of plasmids to ventricles, then dissected in Hank's Buffered Salt Solution (HBSS) supplemented with HEPES (10mM, pH7.4). Tissues were incubated in HBSS containing papain (Worthington; 14U/ml) and DNase I (100 μg/ml) for 15min at 37°C. Then, samples were washed 3 times with HBSS containing DNase I, and dissociated by gentle pipetting. Dissociated cells (8.5×10^4) were plated on poly-D-lysine (1mg/ml, Sigma)-coated glass bottom dishes (MatTek, 35mm dishes with 14mm glass diameter) in Neurobasal media (Invitrogen) containing B27 (1x), Glutamax (1x), FBS (2.5%) and penicillin/streptomycin (0.5x) (all supplements were from Invitrogen). After 5 to 7 days, media were changed with FBS-free supplemented Neurobasal medium.

Structural modeling
Structural homology search for, and corresponding structural homology modeling based on PDB structures mapping to PDZD8 and Mmm1 was performed through the Phyre2 web portal (*56*). Structural analysis, tertiary alignments and visualizations of the E-syt2 (4P42) and Mdm12 (5gyk) PDB structures and SMP-domain homology models generated for PDZD8 and Mmm1 was carried out with PyMOL Molecular Graphics System (Version 1.8 Schrödinger, LLC).

Yeast strain construction
S. cerevisiae strains for *mmm1Δ*-rescue experiments were derived from the heterozygous *mmm1Δ/MMM1* diploid strain YLL006W (BY4743; MATα/α, *his3Δ1/his3Δ1, leu2Δ0/leu2Δ0, LYS2/lys2Δ0, met15Δ0/MET15, ura3Δ0/ura3Δ0*) from the Yeast Knockout Collection (GE Healthcare Dharmacon Inc.). All other strains were derived from from wild-type BY4741 (MAT**a** *his3Δ0, leu2Δ0, met15Δ0* and *ura3Δ0*) from Open

Biosystems (Huntsville, AL). C-terminal tagging of yeast endogenous proteins with fluorescent proteins was performed through homologous recombination as previously described (*57*). Briefly, PCR-fragments with 40bp-flanking regions homologous to 40bp upstream and downstream of pertinent stop-codons, containing mCherry or mTFP1 ORFs followed by suitable selectable markers were generated from plasmids pCY3080-07 (Addgene) and pFA6:mTFP1:kanMX (available upon request). Transformations were performed using the lithium acetate method (ref). Transformants were selected on suitable auxotrophic medium or medium containing $300\,\mu$g ml–1 Hygromycin B (for hphMX4) (Life Technologies, Carlsbad, CA).

Sporulation and tetrad dissection to derive haploid strains from *mmm1Δ*:KanMX6/*MMM1*, *CIT1*-mCherry: hphMX4/CIT1 diploid strains containing pRESC with a pertinent test-construct was carried out according to previously published protocols (*58*). Briefly, cells were incubated in sporulation medium (SPO) on a rotating wheel for 7 days. Asci were digested in 1M sorbitol with 2.5mg/ml zymolase (Seikagaku Corp., Tokyo Japan) for 7 min and tetrad dissection was carried out on SE -URA dropout plates containing $200\,\mu$g ml–1 Geneticin (for KanMX6) (Sigma-Aldrich) or $300\,\mu$g ml–1 Hygromycin B (for hphMX4). Haploid status and correct segregation of genomic alleles and plasmids was confirmed by PCR. Plasmids were cured on 5-FOA plates (SC supplemented with 50 μg ml–1 Uracil and 1% 5-Fluoroorotic acid (5-FOA; Sigma-Aldrich, St Louis, MO)). Single colonies were picked and grown in 5-FOA liquid medium.

Yeast growth conditions
Yeast strains were grown and handled as previously described (*59*). All cells were grown at 30 °C (shaking for liquid cultures) in synthetic complete (SC) medium, unless otherwise stated. For strains requiring selection, appropriate SC dropout medium was used. All imaging was carried out during logarithmic phase.

pRESC construction
pRESC was derived from p416TEF (ATCC® 87368™) by replacing the TEF-promoter with 1000bp directly upstream of the MMM1-ORF. Rescue inserts were derived by PCR or synthesized by GENEWIZ® (South Plainfield, NJ).

Staining of mitochondrial DNA using DAPI
mtDNA was visualized by DAPI staining in live cells in SC containing 1 μg/ml DAPI. Cells were stained for 10 min shaking at room temperature, washed three times, and imaged immediately.

Yeast microscopy and image analysis
Fluorescent microscopy was carried out one of the following microscopes: an Axioskop 2 microscope with 100x/1.4 Plan-Apochromat objective (Zeiss, Thornwood, NY) and an Orca ER cooled CCD camera (Hamamatsu) or an inverted AxioObserver.Z1 microscope with a 100x/1.3 oil EC Plan-Neofluar objective (Zeiss, Thornwood, NY) and Orca ER cooled CCD camera (Hamamatsu, Bridgewater, NJ). Images were collected through the entire cell depth (21 z-sections at 0.3-μm intervals) and deconvolved using an iterative

restoration algorithm (Volocity, Perkin-Elmer, Waltham, MA). Budding cells stained with DAPI were scored for presence of mitochondrial DNA that co-localizes with mitochondria in 3-dimensional reconstructions. To avoid errors due to incidental co-localization of mitochondria with nuclei in dividing cells, cells with less than three individual DAPI foci co-localizing with mitochondria were scored as rho^0. Mitochondrial inheritance dynamics was analyzed in budding cells expressing Cit1p-mCherry with daughter-cell diameters smaller than two-third of the mother-cell (small-to-medium buds). Mitochondrial morphology was analyzed by classifying mitochondrial objects in three categories based on geometric parameters. To this end, mitochondrial objects were detected, and mitochondrial volumes and skeletons were derived in Volocity using inbuilt algorithms. The tubularity of mitochondrial objects was determined by calculating the tubular radius (d) of an ideal cylinder (**Fig. S5A**) based on the determined volume (V) and skeletal length (h) as:

$$\sqrt{\frac{V}{\pi h}} = r$$

Mitochondrial objects were defined as *tubular* if the skeletal length $h \geq 2.5r$ and *spherical* if $h < 2.5r$ (**Fig. S5A-C**). As this simple classifier fails for very small objects (**Fig. S5C**), mitochondria were categorized as *fragmented* regardless of tubularity, if their skeletal length was less than 0.325μm. During normal mitochondrial inheritance in WT cells, mitochondria accumulate at the daughter-cell tip and form aggregates that would be classified as spherical (**Fig. S5D**). To avoid this confounding factor, mitochondrial morphology was analyzed in mother cells only.

Western blotting
Cells were lysed with RIPA buffer (50mM Tris-HCl pH7.2, 500mM NaCl, 1% Triton X-100, 0.5% Sodium deoxycholate, 0.1% SDS, 10mM MgCl$_2$) supplemented with the cocktail of protease inhibitors (Roche), and Benzonase (EMD Millipore) at 37°C for 30min. Samples were loaded onto SDS-PAGE gels and transferred to polyvinylidene difluoride (PVDF) membrane (Amersham). After transfer, membranes were blocked for 1 h with blocking buffer (Li-Cor technology), followed by incubation with primary antibodies overnight at 4°C. The membranes were washed four times with 0.1% TritonX100/PBS and incubated with fluorescent secondary antibodies (Li-Cor technology) for 1 h at room temperature, followed by four times washes with 0.1% TritonX100/PBS. The membranes were scanned by Odyssey® CLx Imaging System (Li-Cor technology). Primary antibodies are rabbit anti-PDZD8 (1:500, in **Fig. 1E** and **Fig. S7A**) (*24*) , rabbit antiserum against a peptide corresponding to a.a. 1103-1119 of mouse PDZD8 (DQHSKKMNKYADDTEED) raised by Covance (1:500, in **Fig. 6B**), chicken anti-GFP (1:2000, GFP-1020; Aves labs), mouse anti-HA (1:2000, clone 16B12, BioLegend), mouse anti-actin (1:5000, Millipore), rabbit anti-VDAC1 (1:500, #4866, Cell Signaling Technology), rabbit anti-MCU (1:500, HPA016480, Sigma Aldrich), and rabbit anti-PTPIP51 (1:1000, A5820, ABclonal).

Quantitative RT-PCR

Cortical neuron culture was infected with lentivirus carrying either the control or shPDZD8 at 4 DIV. RNA was isolated at 13DIV with NucleoSpin® RNA (MACHEREY-NAGEL) according to the instructions of the manufacturer. cDNA was reverse transcribed using SuperScript® III First-Strand Synthesis SuperMix for qRT-PCR (Life Technologies) according to the directions of the manufacturer. The resulting cDNA was analyzed using quantitative PCR with Power SYBR® Green PCR Master Mix (Life Technologies) in an Eppendorf Realplex using the following primers:

Actin
5'- GGCTGTATTCCCCTCCATCG -3'
5'- CCAGTTGGTAACAATGCCATGT-3'
Mouse PDZD8
5'- TTGACATAGAAGCCTGCCATAG -3'
5'- GACATCCTAAAGCCACTTCCTC -3'

Organelle fractionation

Isolation of ER, mitochondria, and MAM from HEK293T cells and PDZD8-Venus knock-in Neuro2a cells was performed following the previously described protocols (*3, 60, 61*). HEK293T cells or Neuro2a cells were harvested from 50 dishes (10cm) at 90-100% confluence and homogenized in isolation buffer (225mM mannitol, 75mM sucrose, 0.1mM EGTA, 30mM Tris-HCl pH7.4) using a Teflon pestle until 80-90% of cells were broken. Then, the homogenate was centrifuged at 600g for 10min twice for removing nuclei and debris. Collected supernatant was centrifuged for 15min at 7000g for obtaining crude mitochondria. For ER isolation, this step was repeated with the supernatant until a pellet is no longer visible, and the supernatant was centrifuged at 20,000g for 30min. Then, the mitochondria-free supernatant was centrifuged again at 100,000g for 1h and the pellet was resuspended for the ER fraction and the supernatant was kept for the cytosolic fraction. For pure mitochondria and MAM fraction, the crude mitochondria pellet was resuspended in 4x-5x volume resuspension buffer (250mM mannitol, 5mM HEPES pH7.4, 0.5mM EGTA), and the fraction was added on the top of 30% percoll medium (225mM mannitol, 25mM HEPES pH7.4, 1mM EGTA, 30% percoll (v/v)) in a centrifuge tube. Centrifuge was performed at 95,000g for 30min, and then the upper (MAM) and lower layer (pure mitochondria) were collected with a Pasteur pipette. Both fractions were diluted with 10x volume resuspension buffer and centrifuged at 6,300g for 15min. Then, the pure mitochondria fraction was obtained from the pellet after one more wash with the same condition. The supernatant containing the MAM was centrifuged at 100,000g for 1h and the resulting pellet was resuspended in resuspension buffer. Western blot was performed using chicken anti-GFP (1:2000, GFP-1020; Aves labs), rabbit anti-PDZD8 (1:500), mouse anti-Calnexin (1:500, 610523; BD bioscience), and mouse anti-cytochrome C (1:1000, 556433; BD bioscience) antibodies.

Confocal imaging

Samples were imaged with either a 20x (0.75 NA) air objective or 60x (1.4 NA) oil objective on a Nikon Ti-e inverted microscope equipped with a Nikon A1 confocal.

Immunohistochemistry

Following anesthesia, mice were heart perfused with 5ml of phosphate buffered saline (PBS 0.1M) and subsequently with 40ml of the fixative solution containing 2% paraformaldehyde (EM grade, EMS) and 0.025% of Glutaraldehyde (GA, EMS) diluted in PB. Brains were then dissected out and post-fixed in the same fixative solution for 3 hours. After embedded in low melting agarose (3%, MP Biomedicals), brains were sectioned at 100μm thickness with a Leica VT1200S vibratome. Sections were treated with ice cold methanol for 6' and blocked with 2% goat serum/PBS for 30 min followed by incubation with anti-GFP at 4ºC overnight. Sections were then washed with PBS followed by treatment with anti-chicken Alexa-488 and mounted with Aqua-Poly/Mount (Polysciences).

Electron microscopy

HeLa cells and PDZD8 KO HeLa cells were fixed with 2% glutaraldehyde (EMS) in 0.1M Phosphate buffer, pH7.4 for 1h at room temperature. After washing with 0.1M Phosphate buffer, cells were scraped and collected with 0.2% BSA/0.1M phosphate buffer followed by centrifugation at 3000 rpm. The samples were post-fixed with 1% OsO_4, 1.5% potassium ferricyanide in 0.1M Phosphate buffer for 1 hour. After 3 times rinse with distilled water, cells were stained with 10% thiocarbohydrazide for 5min followed by incubation with 1% aqueous uranyl acetate for 30 min at room temperature. The samples were rinsed in water, dehydrated in an ethanol series and then infiltrated and embedded in Epon resin (*62*).

The sample block was trimmed then mounted on a SEM sample holder using double-sided carbon tape (EMS). Colloidal silver paint (EMS) was used to electrically ground the exposed edges of the tissue block. The entire surface of the specimen was then sputter coated with a thin layer of gold/palladium. The tissue was imaged using back scattered electron (BSE) mode in a FEI Helios Nanolab 650. Images were recorded after each round of ion beam milling using the SEM beam at 2keV and 100pA with a working distance of 4.0 mm. Data acquisition occurred in an automated way using the Auto Slice and View G3 software. The raw images were 2,048x1,768 pixels, with 20 nm slices viewed at a -38 degree cross-sectional angle. Each raw image had a horizontal field width (HFW) of 15 μm with an XY pixel size of 7-9 nm and 20 nm Z slices. These images were then aligned using the image processing programs in IMOD (*63*).

Analysis of 3D-SEM imaging

3D-SEM images were manually segmented with a Fiji plug-in Track-EM2. Segmented images were imported to Imaris (Bitplane) and analyzed with Surface-Surface contact plug-in. In Imaris, surface-area and volume were calculated using the Statistics feature. The area of ER analyzed was chosen based on localization in region containing the mitochondrial network which was also reconstructed systematically.

ER Three-way Junction Quantification

Three-way junctions in the 3D-SEM images of ER were quantified using a Fiji plug-in Track-EM2. Three-way junctions were identified at points where three distinct ER segments branched from. Quantification of three-way junctions was normalized by the

surface area of the ER that was analyzed. The area of ER analyzed was chosen based on localization to the mitochondrial network.

Calcium imaging

NIH3T3 cells were plated and transfected with plasmids with Jetprime or FugeneHD (Promega). Cells were replated on glass bottom dishes (MatTek) at $1\times10^4/cm^2$ density and incubated for 1 day. The medium was replaced with Hank's buffered salt solution (HBSS) supplemented with HEPES (pH7.4; 2.5mM), $CaCl_2$ (2mM, Sigma), $MgSO_4$ (1mM, Sigma), $NaHCO_3$ (4mM, Sigma), and D-glucose (30mM, Sigma). Cells were stimulated with $200\mu M$ ATP (Sigma Aldrich, A1852) and imaged with an inverted Nikon Ti-E microscope equipped with EMCCD camera (Andor, iXon3-897), 20x objective (0.75NA). 470nm, 555nm, and 360nm Spectra X LED lights (Lumencor) were used for the light source, and a custom quad-band excitation/mirror/emission cube (based off Chroma, 89400) followed by clean up filters (Chroma, ET525/50, ET600/50, ET435/26) were applied for excitation and emission.

For experiment with permeabilized cells (**Fig. S9**), cells were treated with $2.5\mu M$ digitonin (Sigma-Aldrich) and $20\mu M$ cyclopiazonic acid (CPA; Tocris) in intracellular buffer (130mM KCl, 10mM NaCl, 2mM K_2HPO_4, 5mM succinic acid, 1mM $MgCl_2$, 20mM HEPES) for 3min before imaging. After 10s of imaging, cells were stimulated by application of a solution containing 1mM $CaCl_2$ and imaged for another 20s. To confirm the Ca^{2+} uptake is mediated by MCU, cells were treated with MCU inhibitor $10\mu M$ RU360 (Calbiochem).

For neuronal calcium imaging, electroporated cortical neurons were imaged using the same microscope (40x objective NA 0.95) with an EMCCD (Andor, iXon3-897) camera at 19-22DIV. 470nm and 555nm LED lights were applied for the light source, and the same cube and clean up filters (Chroma, ET525/50, ET600/50) were used for dual color imaging. We imaged neurons in modified normal tyrode solution (145mM NaCl, 2.5mM KCl, 10mM HEPES pH7.4, 2mM $CaCl_2$, 1mM $MgCl_2$, 10mM glucose) at 37°C (Tokai Hit Chamber). Electrical stimulation is triggered by 1ms current injections with a concentric bipolar electrode (FHC) placed 50-100µm away from transfected neuronal cell bodies for stimulating nearby axons. We applied 20APs (10Hz) with 30V using the stimulator (Model 2100, A-M systems) and imaged with 500ms interval (2Hz) during 90sec for G-CEPIA1er, mito-RCaMP1h, and cyto-RCaMP1h signals. For CEPIA3mt imaging, 100ms interval (10Hz) was applied during 40s. For blocking SERCA pump, NMDAR, or mGluR1, cyclopiazonic acid (CPA, $30\mu M$ for 5min; Tocris), APV ($50\mu M$ for 3min; Tocris), or LY367385 ($100\mu M$ for 10min; Sigma-Aldrich) were incubated, respectively.

Images were analyzed using the NIS Elements software (Nikon) or a Fiji (Image J) plug-in, Time Series Analyzer (v3.0). One small area of each Hela cell is selected by circular ROI by NIS Elements, and average intensities were measured with background correction. 2-3 dendritic segments ($10\mu m$) from a single neuron and nearby backgrounds were selected by ROIs and average intensities were measured by the plug-in. After intensities were corrected for background subtraction, ΔF values were calculated from $(F-F_0)$. F_0 values were defined by averaging 10 frames before stimulation, and used for normalization. For F_{max} values, ionomycin ($5\mu M$) were applied after stimulation and average intensity of 10 frames from a plateau was employed for normalization.

TMRM imaging

NIH3T3 cells were plated and transfected with pCAG-mitoYFP and either control plasmid (pLKO1) or pLOK1 vector expressing shRNA targeting *Pdzd8* plasmids with FugeneHD (Promega). Cells were replated on glass bottom dishes (MatTek) at $1x10^4/cm^2$ density and incubated for 1 day. After treatment with 20nM TMRM for 20min, the medium was replaced with Hank's buffered salt solution (HBSS) supplemented with HEPES (pH7.4; 2.5mM), $CaCl_2$ (2mM, Sigma), $MgSO_4$ (1mM, Sigma), $NaHCO_3$ (4mM, Sigma), and D-glucose (30mM, Sigma) and 5nM TMRM. Cells were imaged with 60x (1.4 NA) oil objective on a Nikon Ti-e inverted microscope equipped with a Nikon A1 confocal. To obtain eliminate mitochondrial membrane potential, cells were treated with $0.3\mu M$ FCCP (Enzo Life Sciences) and $1\mu g/\mu l$ Oligomycin (Calbiochem).

In utero cortical electroporation

The *in utero* electroporation method was performed as previously described. Briefly, a mixture of the vectors pCAG Canx-YFP and pCAG mito (CoxVIII)-mtagBFP2 together with either control pLKO vector or pLKO-shPDZD8 were injected into the neocortical lateral horn of embryos obtained from a timed-pregnant CD1 mouse female at E15.5 with Picospritzer III (Parker, Hollis NH, USA). The cDNA mixtures were then electroporated into the neural progenitor cells resided in the ventricular zone by 5 electric pulses (50ms) of 38V using Tweezer-type platinum electrode (diameter 3mm; NEPA GENE) and an electroporation system ECM 830 (BTX, Holliston MA, USA).

In situ hybridization

In situ hybridization was performed as previously described (*64*). The probes for PDZD8 was generated with the following primers;
5'- GCGAATTAACCCTCACTAAAGGGTTCCTTCAGAAAGTTCTGCTCC -3'
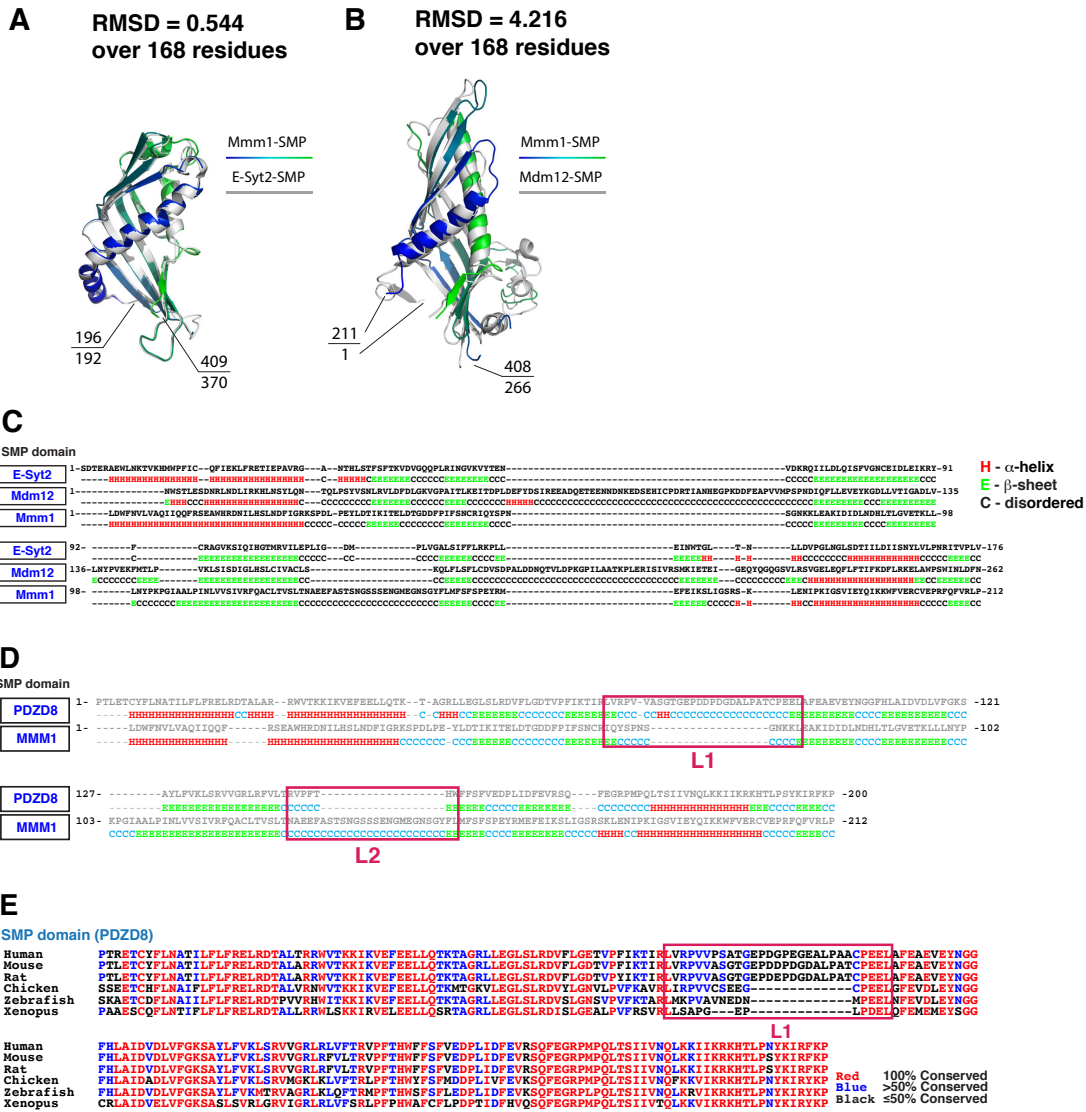5'- GCGTAATACGACTCACTATAGGGGTCTATTCGCCTCTCAGTTGCT -3'

A RMSD = 0.544 over 168 residues

Mmm1-SMP
E-Syt2-SMP

196
192
409
370

B RMSD = 4.216 over 168 residues

Mmm1-SMP
Mdm12-SMP

211
1
408
266

C

SMP domain

H - α-helix
E - β-sheet
C - disordered

E-Syt2 1-SDTERAEWLNKTVKHMWPPIC--QFIEKLFRETIEPAVRG---A--NTHLSTFSFTKVDVGQQPLRINGVKVYTEN--VDKRQIILDLQISFVGNCEIDLEIKRY-91
----------------HHHHHHHHHHHH---HHHHHHHH---C--HHHHHCEEEEEECCCCCCEEEEECCC--CCCCEEEEEEEEEEEEEEECCC

Mdm12 1---------------NVSTLESDNRLNDLIRKHLNSYLQN----TQLPSYVSNLRVLDFDLGKVGPATTLKEITDPPLDEFYDSIREEADQETEENNDNKKEDSEHICPDRTIANHEGPKDDPEAPVVMPSPNDIQFLLEVEYKGDLLVTIGADLV-135
-----EEHHCCCCCCCCCCCCCCCCCCCEEEEEEECCC----CCCCCCCCCCCCCCCCCCCCCCCCCCCCCCCCCCCCCCCCCCCCCCCCCCCCCCCEEEEEEEECCCEEEEEEEE

Mmm1 1-----LDWFNVLVAQIIQQFRSEAWHRDNILHSLNDFIGRKSPDL--PEYLDTIKITELDTGDDPFIFSNCRIQYSPN--SGNKKLEAKIDIDLNDHLTLGVETKLL--98
-----HHHHHCC-----HHHHHHHHHHHHHCCCCCCEEEEEEEECCEEEEEEEEC--SGNKKLEAKID...EEEEEECCCCEEEEEEE

E-Syt2 92-------F-------CRAGVKSIQIHGTMRVILEPLIG--DM----------PLVGALSIFFLRKPLL---------------------------------EINWTGL----T--N--------LLDVPGLNGLSDTIILDIISNYLVLPNRITVPLV-176
-------C---------EEEEEEEEEEEEEEEEEECCCCCC----------CCCCEEEEEEEE---------------------------------EEEHH--H--N--------HHCCCCCCCCCCHHHHHHHHHHHHHEEECCCCEEE

Mdm12 136-LNYPVEKFMTLP-------VKLSISDIGLHSLCIVACLS-----------------KQLFLSFLCDVSDPALDDNQTVLDPKGPILAATKPLERISIVRSMKIETEI---GEQYQGQGSVLRSVGELEQFLFTIFKDPLRKELAWPSWINLDFN-262
-CCCCCCEEEEEE------EEEEEESIDIGLHSLCIVACLS-----------------CCCCCC----------------EEEEHH--H--N--------HHCCCCCCCCCCHHHHHHHHHHHHHEEECCCCEEE

Mmm1 98-------LNYPKPGIAALPINLVVSIVRFQACLTVSLTNAEEFASTSNGSSSENGMEGNSGYFLMFSFSPEYRM----------------------EFEIKSLIGSRS-K------LENIPKIGSVIEYQIKKWFVERCVEPRFQFVRLP-212
-------NCCCCCCEEEEEEEEEEEEEEEEEECCCCCCCCCCCCCCCCCCCCCCCCCCEEEEECCEE------------------------EEEEECCCCH--H-------HHCCHHHHHHHHHHHHHHHHHCCCCCEEEECC

D

SMP domain

PDZD8 1- PTLETCYFLNATILFLFRELRDTALAR--RWVTKKIKVEFEELLQTK--T-AGRLLEGLSLRDVFLGDTVPFIKTIR|LVRPV-VASGTGEPDDPDGDALPATCPEEL|AFEAEVEYNGGFHLAIDVDLVFGKS -121
----HHHHHHHHHHHHHHHHHCCHHHH--HHHHHHHHHHHHHHHHHH--C-CHHHCCEEEEEEECCCCCCCEEEEEBECCC-CCHHCCCCCCCCCCCCCCCCCEEEEEEECCCCCEEEEEEEECCC

MMM1 1- -----LDWFNVLVAQIIQQF------RSEAWHRDNILHSLNDFIGRKSPDLPE-YLDTIKITELDTGDDPFIFSNCR|IQYSPNS----------------GNKKL|EAKIDIDLNDHLTLGVETKLLLNYP -102
----HHHHHHHHHHHHHHH----HHHHHHHHHHHHHHHHHHCCCCCCEEEEEEBC-----------------CCCCC-EEEEEEEECCCEEEEEEEEEEEEECCC

L1

PDZD8 127- --------AYLFVKLSRVVGRLRFVLT|RVPFT------------------HW|FSFVEDPLIDFEVRSQ----FEGRPMPQLTSIIVNQLKKIRKHTLPSYKIRFKP -200
--------EEEEEEEEEEEEEEEEEBCCCCC------------------EEBEEECCCCEEEEEEE----HHHHHHHHHHHHHHHHHHHHHHHCCCCCEEEECC

MMM1 103- KPGIAALPINLVVSIVRFQACLTVSL|NAEEFASTSNGSSSENGMEGNSGYFL|MFSFSPEYRMEFEIKSLIGSRSKLENIPKIGSVIEYQIKKWFVERCVEPRFQVRLP -212
CCCCEEEEEEEEEEEEEEEEEEBC-CCCCCCCCCCCCCCCCCCCCCCCBEBGSBRCCCCEEEEEEEEBCCCCHHHHHCCHHHHHHHHHHHHHHHHHHHHHCCCCCEEEECC

L2

E

SMP domain (PDZD8)

Human PTRETCYFLNATILFLFRELRDTALTRRWVTKKIKVEFEELLQTKTAGRLLEGLSLRDVFLGETVPFIKTIR|LVRPVVPSATGEPDGPEGEALPAACPEEL|AFEAEVEYNGG
Mouse PTLETCYFLNATILFLFRELRDTALARRWVTKKIKVEFEELLQTKTAGRLLEGLSLRDVFLGDTVPFIKTIR|LVRPVVASGTGEPDDPDGDALPATCPEEL|AFEAEVEYNGG
Rat PTLETCYFLNATILFLFRELRDTALRRWVTKKIKVEFEELLQTKTAGRLLEGLSLRDVFLGDTVPYIKTIR|LVRPVVASGTGEPDDPDGDALPATCPEEL|AFEAEVEYNGG
Chicken SSEETCHFLNAIFLFLFRELRDTALVRNWVTKKIKVEFEELLQTKMTGKVLEGLSLRDVLGNVLPVFKAVR|LIRPVVCSEEG-------------CPEEL|GFEVDLEYNGG
Zebrafish SKAETCDFLNAIILFLFRELRDTPVVRHWITKKIKVEFEELLQTKTAGRLLEGLSLRDVFKTAR|LMKPVAVNEDN-------------MPEEL|NFEVDLSYNGG
Xenopus PAAESCQFLNTIFLFLFRELRDTALLRRWLSKKIRVELEELLQSRTAGRLLEGLSLRDISLGEALPVFRSVR|LLSAPG---EP-------------LPDEL|FEMEMEYSGG

L1

Human FHLAIDVDLVFGKSAYLFVKLSRVVGRLRLVFTRVPFTHWFFSFVEDPLIDFEVRSQFEGRPMPQLTSIIVNQLKKIRKHTLPSNYKIRFKP
Mouse FHLAIDVDLVFGKSAYLFVKLSRVVGRLRFVLTRVPFTHWFFSFVEDPLIDFEVRSQFEGRPMPQLTSIIVNQLKKIRKHTLPSYKIRFKP
Rat FHLAIDVDLVFGKSAYLFVKLSRVVGRLRFVLTRVPFTHWFFSFVEDPLIDFEVRSQFEGRPMPQLTSIIVNQLKKIRKHTLPSYKIRFKP
Chicken FHLAIDADLVFGKSAYLFVKLSRVMGRLKLVFTRLPFTHWYFSFMDDPLIVFEVRSQFEGRPMPQLTSIIVNQFKKVIKRKHTLPNYKIRYKP
Zebrafish FHLAIDVDLVFGKSAYLFVKMTRVAGRLKLQFTRMPFTHWSFSFLEDPLIDFEVKSQFEGRPLQLTSIIVNQLKKVIKRKHTLPNYKIRYKP
Xenopus CRLAIDVELVFGKSASLSVRLGRVIGRLRLVFSRLPFPHWAFCFLPDPTIDPHVQSQFEGRPMPQLTSIIVTQLKKVIKRKHTLPNYKIRYKP

Red 100% Conserved
Blue >50% Conserved
Black ≤50% Conserved

Fig. S1 Tertiary, secondary and primary sequence alignment between the SMP domain of PDZD8 and other SMP domains.
(**A, B**) Superimposition of Phyre2 homology models for the SMP domains of Mmm1 (green-blue in A,B) over templates from the crystal structures of either E-Syt2 (white in A, 192-370 a.a.; PDB code 4P42) or Mdm12 (white in B, 1-266 a.a.; PDB code 5gyk). (**C**) Predicted secondary structure of the SMP domain of Mmm1 (*S. cerevisiae)* aligned with the secondary structure of E-Syt2 (human) and Mdm12 (*S. cerevisiae*), another SMP domain-containing protein found in the ERMES complex. (**D**) Secondary structural alignment of a.a. sequences corresponding to the SMP domains of yeast MMM1 and mouse Pdzd8. Predicted secondary structures are shown below the a.a. sequence. Loop regions (L1 and L2) are highlighted by red boxes and show absence of conservation between the two sequences. (**E**) Primary a.a. sequences of PDZD8 SMP domains from indicated species are aligned. Red, blue, and black characters indicate 100%, >50%,

≤50% conservation of the a.a. residues among corresponding species, respectively. Note that L1 loop region (box) is not conserved across the vertebrate species.
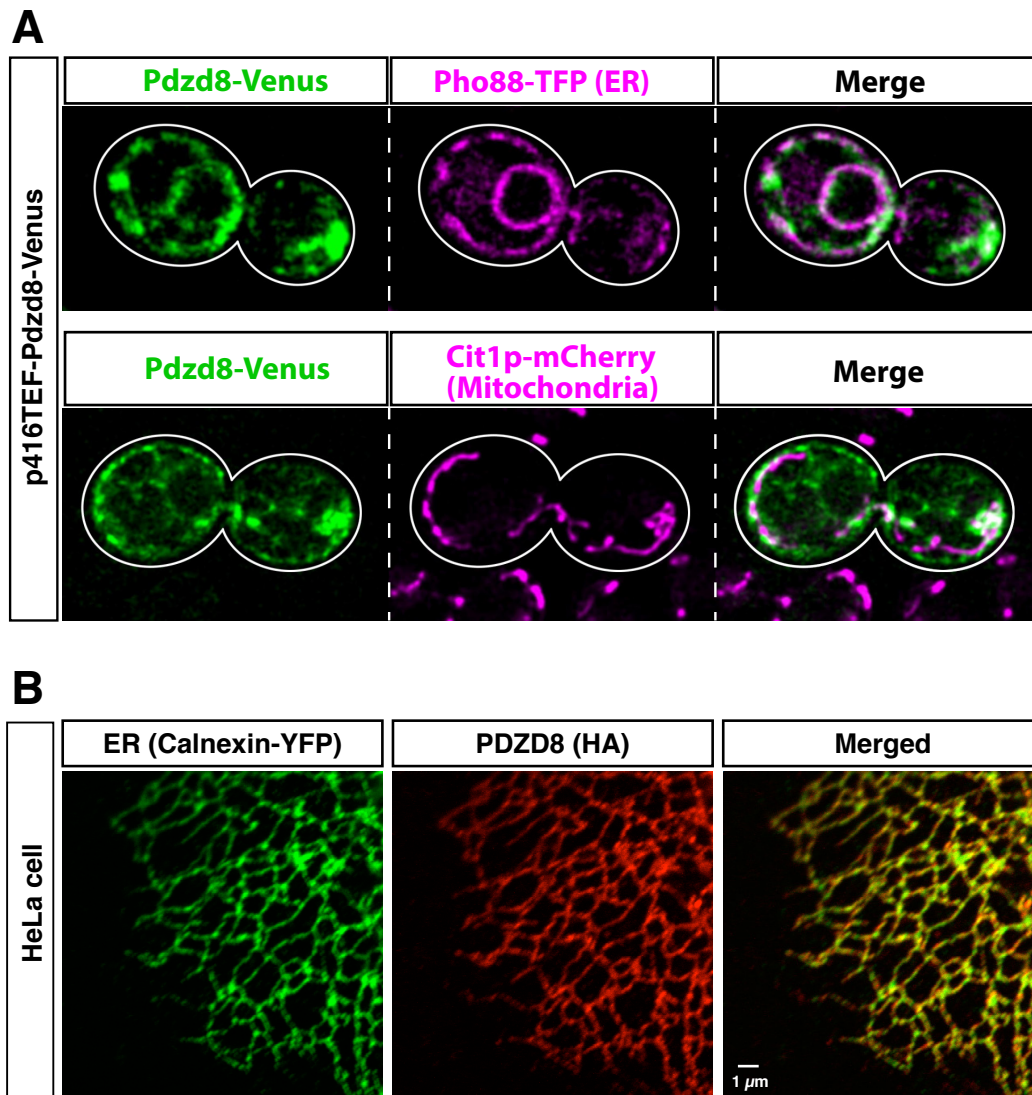
Fig. S2 PDZD8 is localized at ER in yeast and human cells.
(**A**) Plasmid-borne PDZD8-Venus co-localizes with the ER-marker Pho88-TFP, but not the mitochondrial-matrix marker Cit1p-mCherry, both expressed from their endogenous loci. (**B**) Overexpressed HA-tagged PDZD8 localizes at the ER in HeLa cell co-transfected with a plasmid expressing Canx-YFP (ER marker) and stained with anti-GFP and anti-HA antibodies.

A

Strain construction → **Spore-dissection** → **Plasmid-cure**

B

PDZD8

1   353

TM   SMP   PDZ   C1   CC

PDZD8^(TM-SMP)

TM   SMP   HA

PDZD8

92   353

TM   SMP   PDZ   C1   CC

MMM1

TM   191   409

MMM1^(SMP-PDZD8-Full)

C

	CIT1-mCherry (Mitochondria)	DAPI	Merge
pMMM1		N, M	
	5-FOA	5-FOA N	5-FOA
pRESC^empty		N	
pPDZD8^(TM-SMP)		N	
pMMM1^(SMP-PDZD8-full)		N	
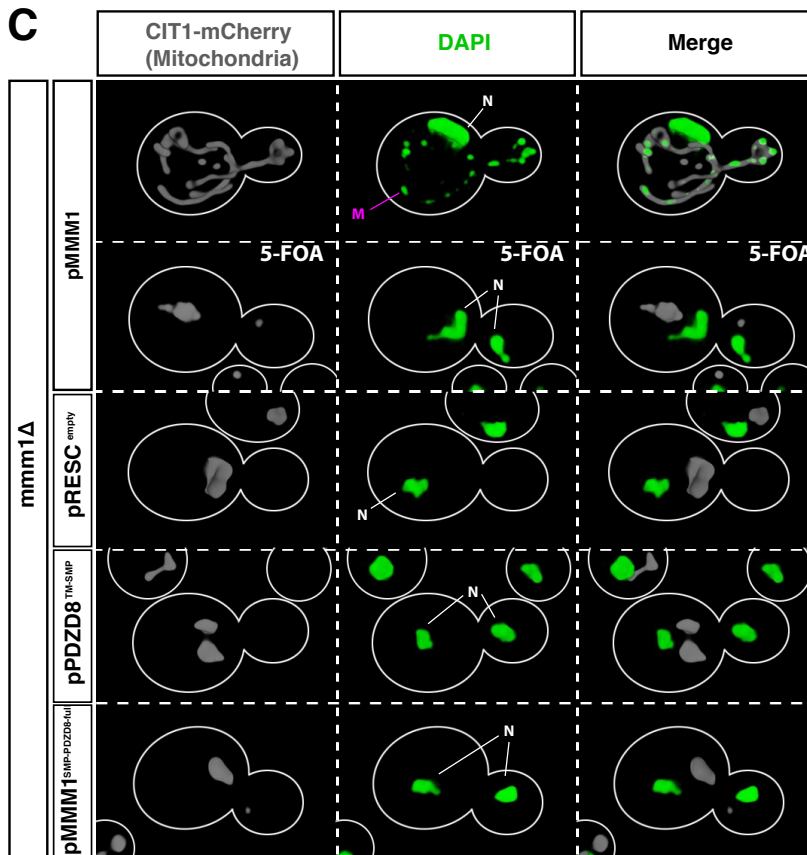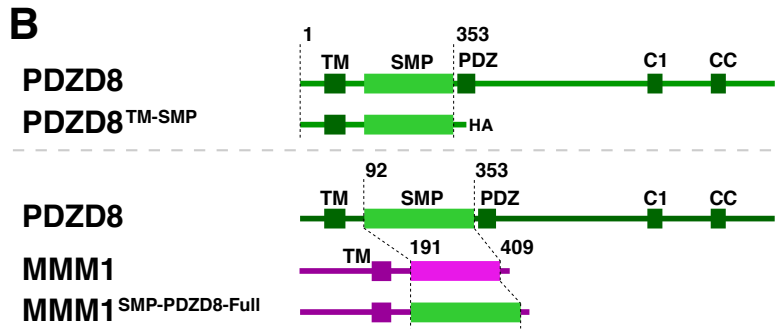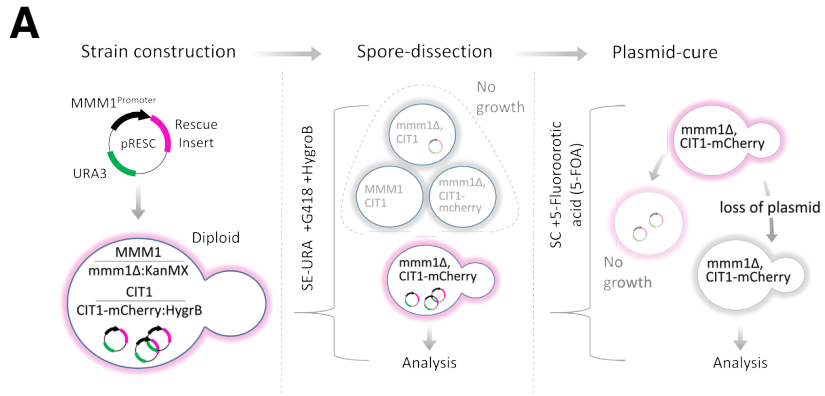
mmm1Δ

Fig. S3 Original SMP domain of PDZD8 is not sufficient to restore the yeast *mmm1Δ* defects.

(**A**) Diagram detailing the experimental strategy. Diploid heterozygotes for *mmm1Δ:KanMX* and *CIT1-mCherry:Hygromycin-B* (for visualizing mitochondria) alleles were transformed with plasmids (pRESC) containing a *URA3*-selection marker and the endogenous *MMM1*-promoter sequence followed by particular cDNA rescue inserts. Tetrad dissection was performed and colonies selected for co-segregation of *mmm1Δ*, *CIT1-mCherry* and pRESC, and analyzed. pRESC was then shuffled out from rescue strains by growth on media containing 5-Fluoroorotic acid (5-FOA), which is toxic to URA3 expressing strains, and assessed for reversion to *mmm1Δ* phenotype. (**B**) Diagrams detailing particular rescue constructs (Mmm1-sequence in magenta shading). (**C**) Rescue of *mmm1Δ* phenotypes by several pRESC constructs was assessed. Representative images (3D opacity rendering) of nuclear (N in white) and mitochondrial (M in magenta) DNA (DAPI) and mitochondria (Cit1p-mCherry) in *mmm1Δ* strains containing pRESC expressing full-length *MMM1* (p*MMM1*), p*MMM1* cells after 5-FOA plasmid cure, empty pRESC plasmids; pRESC expressing an N-terminal fragment of PDZD8 containing its TM and SMP domain (pPDZD8^{TM-SMP}), and MMM1 containing PDZD8-SMP domain (p*MMM1*$^{SMP-PDZD8-Full}$). Cell outlines are shown in white.

Fig. S4 PDZD8-SMP domain containing L1 and L2 loops from Mmm1 rescues the yeast *mmm1Δ* defects.

(**A**) Diagrams detailing p*MMM1*[SMP-PDZD8+L1L2] (left) and p*MMM1*SMP[-Mdm12+L1] (right) rescue constructs (Mmm1-sequence in magenta shading). (**B**) Structural predictions generated by PDB search through Phyre2 for p*MMM1*[SMP-PDZD8+L1L2] (left) and p*MMM1*SMP[-Mdm12+L1] (right) chimera based on E-syt2 (4P42) template. (**C**) Primary a.a. sequence of Pdzd8+L1L2 (underlined black bold characters) is illustrated. (**D**)

Representative images (3D opacity rendering) of nuclear (N) and mitochondrial (M) DNA (DAPI) and mitochondria (Cit1p-mCherry) in WT, *mmm1Δ*, *mmm1Δ* rescue strains containing p*MMM1-SMP$^{PDZD8+L1L2}$*, or p*MMM1*SMP$^{-Mdm12+L1}$ plasmids and the same strain following plasmid removal with 5-FOA. Cell-outlines are shown in white. Mitochondria falling into *Tubular (T)*, *Spherical (S)* and *Fragment* (F) morphology categories are indicated. **(E)** Proportion of cells (n>100) containing mtDNA (rho$^+$) as identified by DAPI staining, and **(F)** mitochondrial inheritance dynamics as the proportion of small-to-medium sized buds (n>60) containing mitochondrial Cit1-mCherry signal. **(G)** Quantitation of the proportion of mitochondrial objects in budding mother cells (n>100) falling into each mitochondrial morphological category as defined in Experimental Procedures. Statistical significance was determined by Fisher's Exact Test for Count Data. * $p<0.05$, ** $p<0.01$, ***$p<0.005$.

A

$$\sqrt{\frac{V}{\pi h}} = r$$

B

WT   mmm1Δ
······ SkL/TD > 2.5   ······ SkL > 0.325

tubular

spherical

fragmented

Skeletal length (SkL) (μm) vs **Tubular Diameter (TD) (μm)**

C

WT   mmm1Δ

***   p=0.83

Proportion of mitochondria with tubular morphology

SkL > 0.325   SkL < 0.325

D WT Cit1p-mCherry

Daughter Cell

Mitochondria
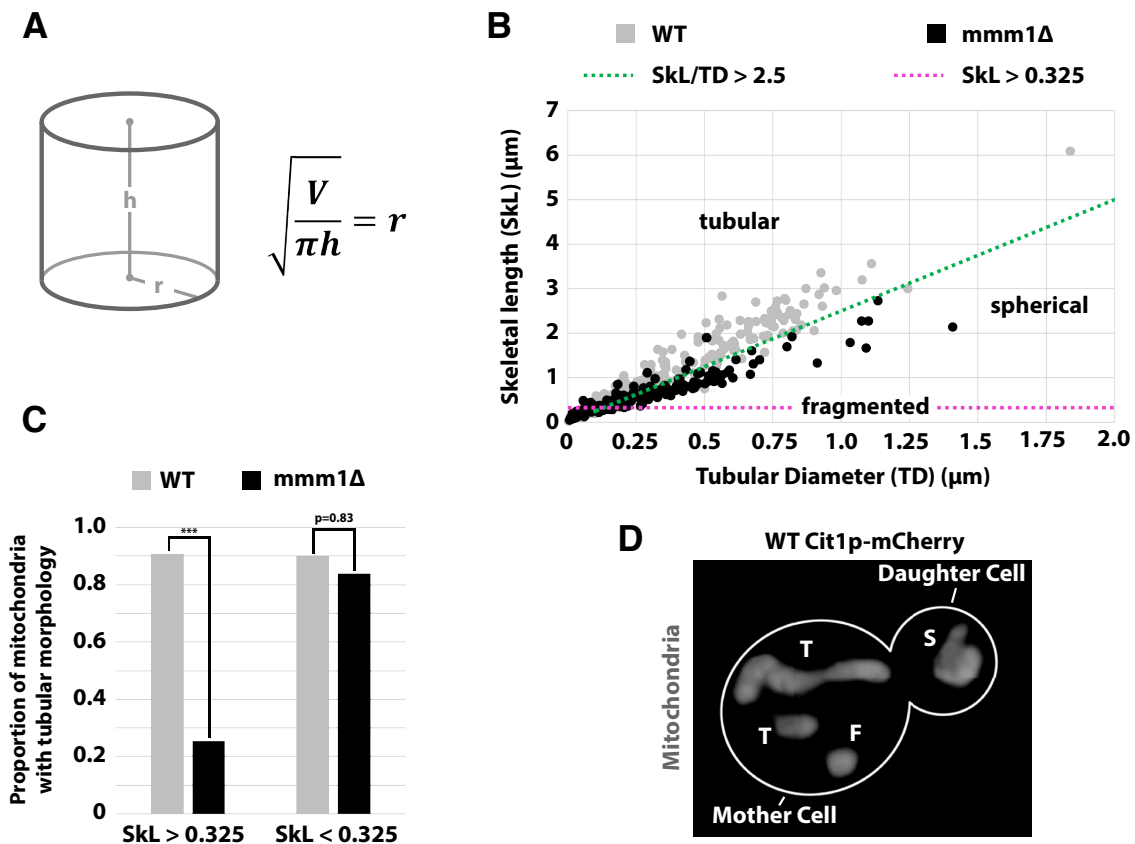
Mother Cell

Fig. S5 Quantitative approaches for measurement of mitochondrial morphology in yeast

(A) Volume and skeletal length (SkL) of mitochondrial objects in budding mother-cells were used to calculate the diameter (d) of an ideal cylinder with equal volume (V) and SkL as height (h). Based on this (d) was defined as the tubular diameter (TD) and **(B)** individual mitochondrial objects from WT and *mmm1Δ* cells were classified as *tubular* for SkL/TD>2.5 and as spherical for SkL/TD <2.5. **(B,C)** The classifier is unable to distinguish objects from WT and *mmm1Δ* cells with SkL<0.325μm according to *tubular* and *spherical* categories and small objects are classified as *fragmented*. **(D)** Representative WT cell expressing Cit1p-mCherry containing examples of all three categories; *tubular* (T), *spherical* (S), *fragmented* (F). Cell outlines are shown in white. Statistical significance was determined by Fisher's Exact Test for Count Data. * $p<0.05$, ** $p<0.01$, ***$p<0.005$.
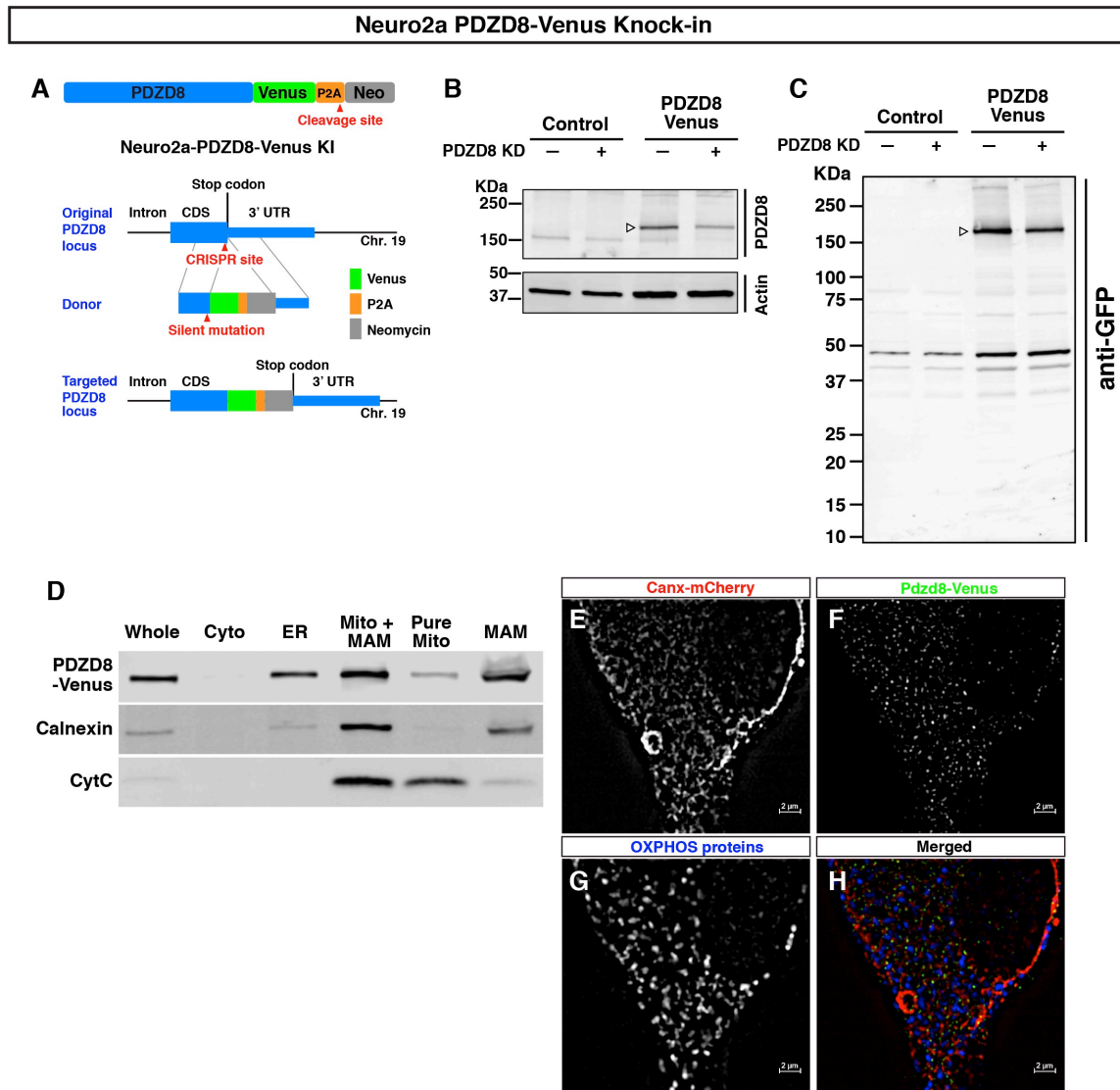
Fig. S6 Validation and analysis of Pdzd8-Venus knock-in Neuro2a cell line

(A) Diagram describing the strategy for making Neuro2a-PDZD8-Venus cell line. (**B-C**) Western blot analysis using anti-PDZD8 antiserum (B) or GFP antibody (C) in PDZD8-Venus-KI-Neuro2a cell line. Cell lysates were collected from control or PDZD8-Venus-KI Neuro2a cells transfected with plasmids expressing either control or *Pdzd8* shRNA. Arrowhead indicates bands corresponding to PDZD8-Venus fusion protein. (**D**) Immunoblot of subcellular fractionation from PDZD8-Venus knock-in Neuro2a (N2a) cells demonstrates the presence of PDZD8 in ER and MAM fractions. MAM fraction was isolated using a Percoll gradient, and immunoblot was performed with anti-GFP for PDZD8-Venus, anti-Calnexin for ER and MAM fraction, and anti-cytochrome C for mitochondrial fraction. (**E-H**) Larger field of view for images detailed in **Fig. 1F-I**. PDZD8-Venus knock-in N2a cells were transfected with a plasmid expressing Calnexin-mCherry (ER marker) and stained with anti-RFP, anti-GFP antibody, and anti-OXPHOS complex antibody (mitochondrial marker). The stained cells were imaged with 3D N-SIM.
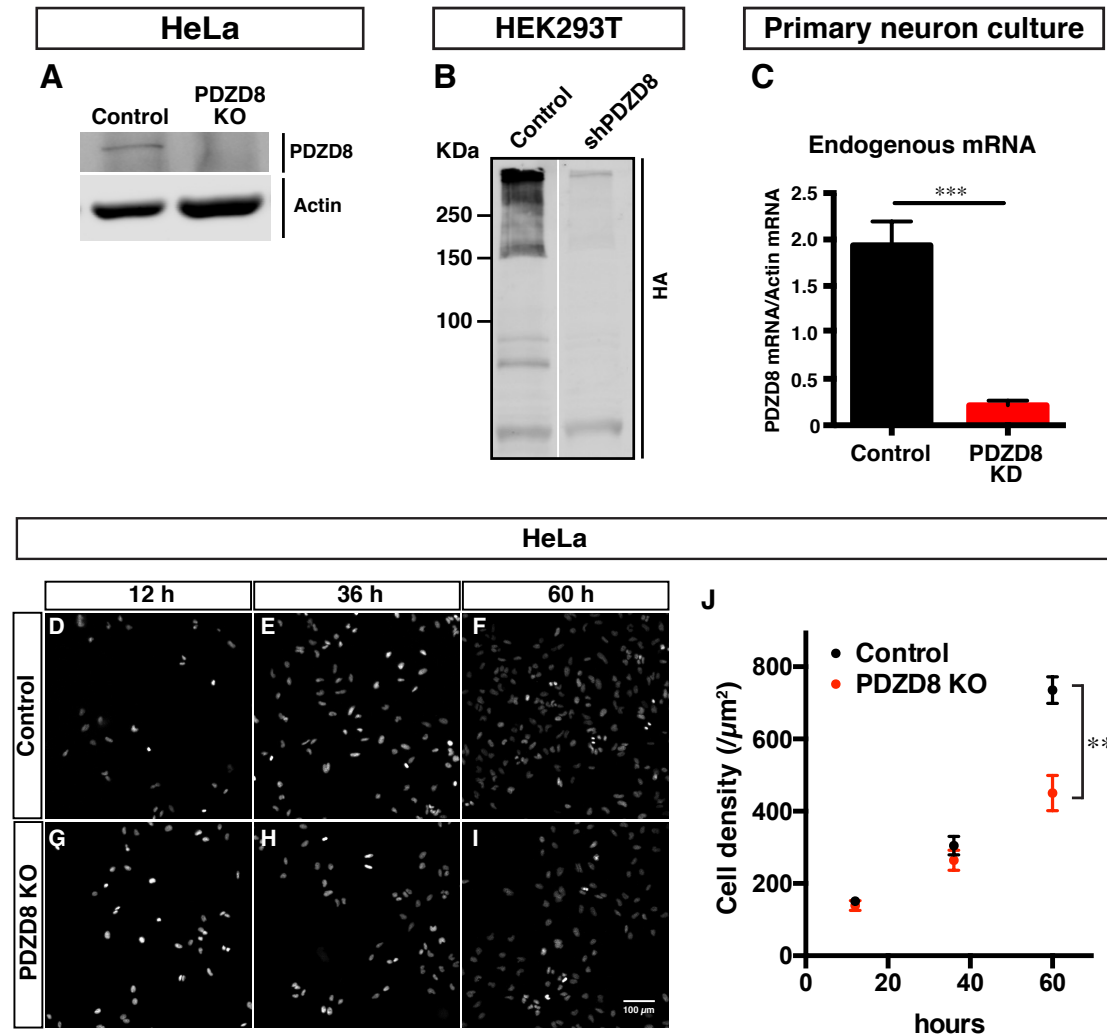
Fig. S7 Validation of *Pdzd8* shRNA knockdown efficacy and PDZD8 knockout HeLa cells.

(**A**) PDZD8 is absent in the PDZD8 KO HeLa cells. Cell lysates collected from control or PDZD8 KO HeLa cells were subjected to Western blotting with anti-PDZD8 and anti-Actin antibodies. (**B**) Efficacy of knockdown using shRNA against mouse *Pdzd8* in HEK293 cells measured by Western blot analysis (**C**). Cultured mouse cortical neurons were infected at 4DIV with lentivirus expressing either control or *Pdzd8* shRNA and total RNA was extracted at 13DIV. The *Pdzd8* mRNA amounts were quantified by quantitative RT-PCR and normalized by *Actin* mRNA levels. (**D-J**) PDZD8 KO decreases the rate of HeLa cell growth. Control or PDZD8 KO HeLa cells were plated at 7.9×10^3 cells/cm^2. (**D-I**) Representative images of the cells with nuclear staining are shown. (**J**) Cell density i.e. number of cells per region of interest was quantified at 12, 36 and 60 hours after plating following longitudinal imaging from the same dishes (n=3). **p<0.005 *** p<0.001, Student's t-test.
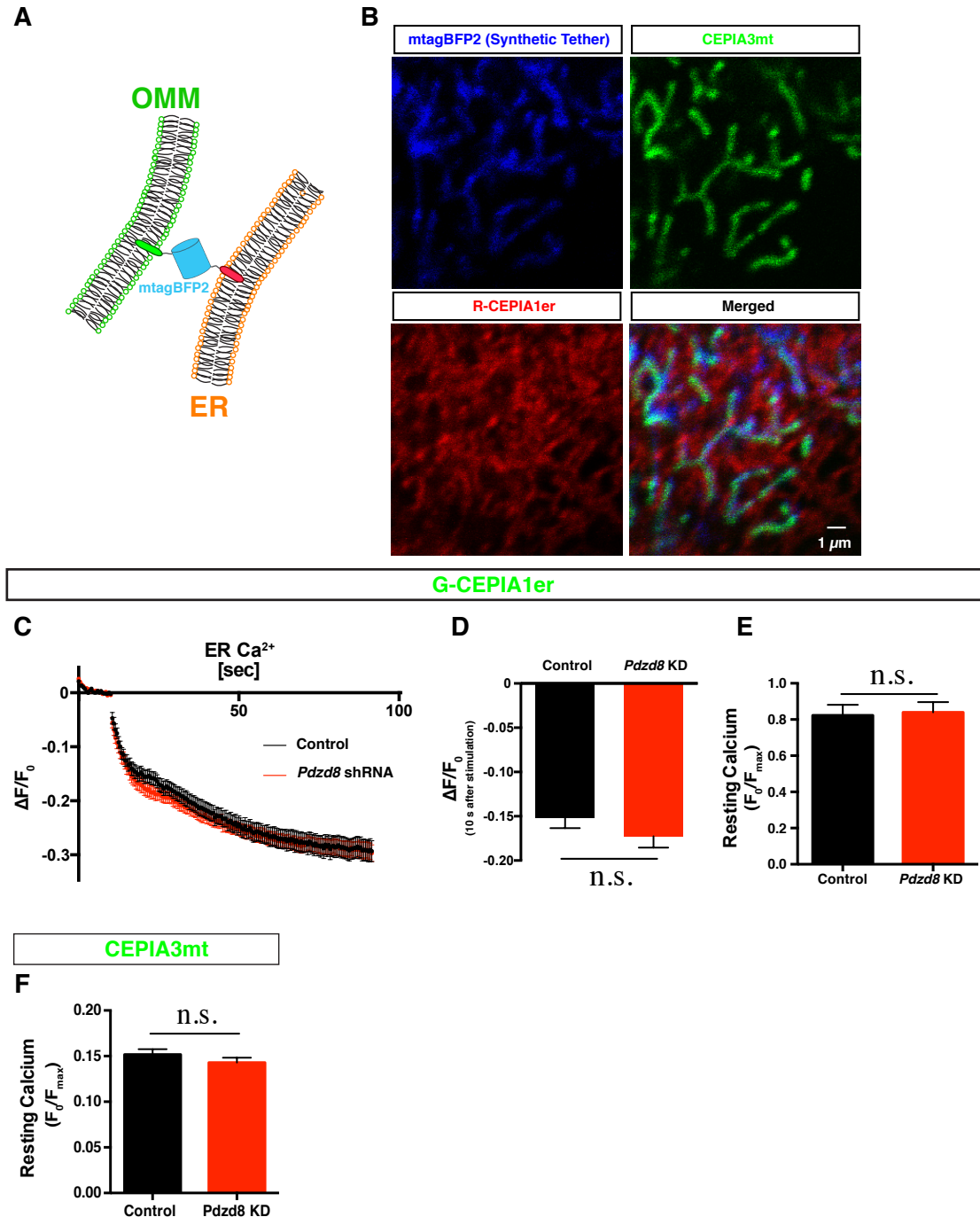
Fig. S8 Localization of synthetic ER-mitochondria tethering construct and measurement of ER Ca^{2+} load and release in NIH3T3 cells.

(**A**) Schematic of the synthetic tethering protein. Green oval; mitochondria targeting domain of mouse AKAP1, Red oval; ER targeting domain of yeast UBC6, Grey line; linker protein. OMM; outer mitochondrial membrane. (**B**) Subcellular localization of the synthetic tethering protein (mTagBFP2; blue) used in Figure 3 along with CEPIA3mt (green), and R-CEPIA1er (red) in NIH3T3 cells was assessed by confocal microscopy

and reveals strong overlap with both mitochondria and ER. (**C-D**) NIH3T3 cells were transfected with plasmids encoding ER-targeted GECI (G-CEPIA1er) together with either a control plasmid (Control) or a *Pdzd8* shRNA plasmid. Cells were stimulated with 200 μM ATP to induce ER Ca^{2+} release and changes in fluorescence from G-CEPIA1er were measured. (C) Changes of G-CEPIA1er fluorescence (ΔF) from normalized by basal signals before ATP stimulation (F_0) are shown. (D) Peak intensities of $\Delta F/F_0$ 10 seconds after ATP stimulation are not significantly different between the control and *Pdzd8* KD cells. n= 37 (Control), 23 (*Pdzd8* KD). (**E-F**) Resting ER (E) and mitochondrial (F) Ca^{2+} levels are measured from basal signals (F_0 i.e. prior to ATP stimulation) normalized by F_{max} obtained following ionomycin (5μM) treatment which allows normalization for potential cell-to-cell variation in GECI expression levels. Resting Ca^{2+} levels are not significantly changed in *Pdzd8* KD NIH3T3 cells compared to control cells. (E) n= 13 (Control), 16 (*Pdzd8* KD), (F) n= 35 (Control), 25 (*Pdzd8* KD). (D, F) n.s. p>0.05 according to Unpaired t-test with Welch's correction. (E) n.s. p>0.05 according to Unpaired t-test.
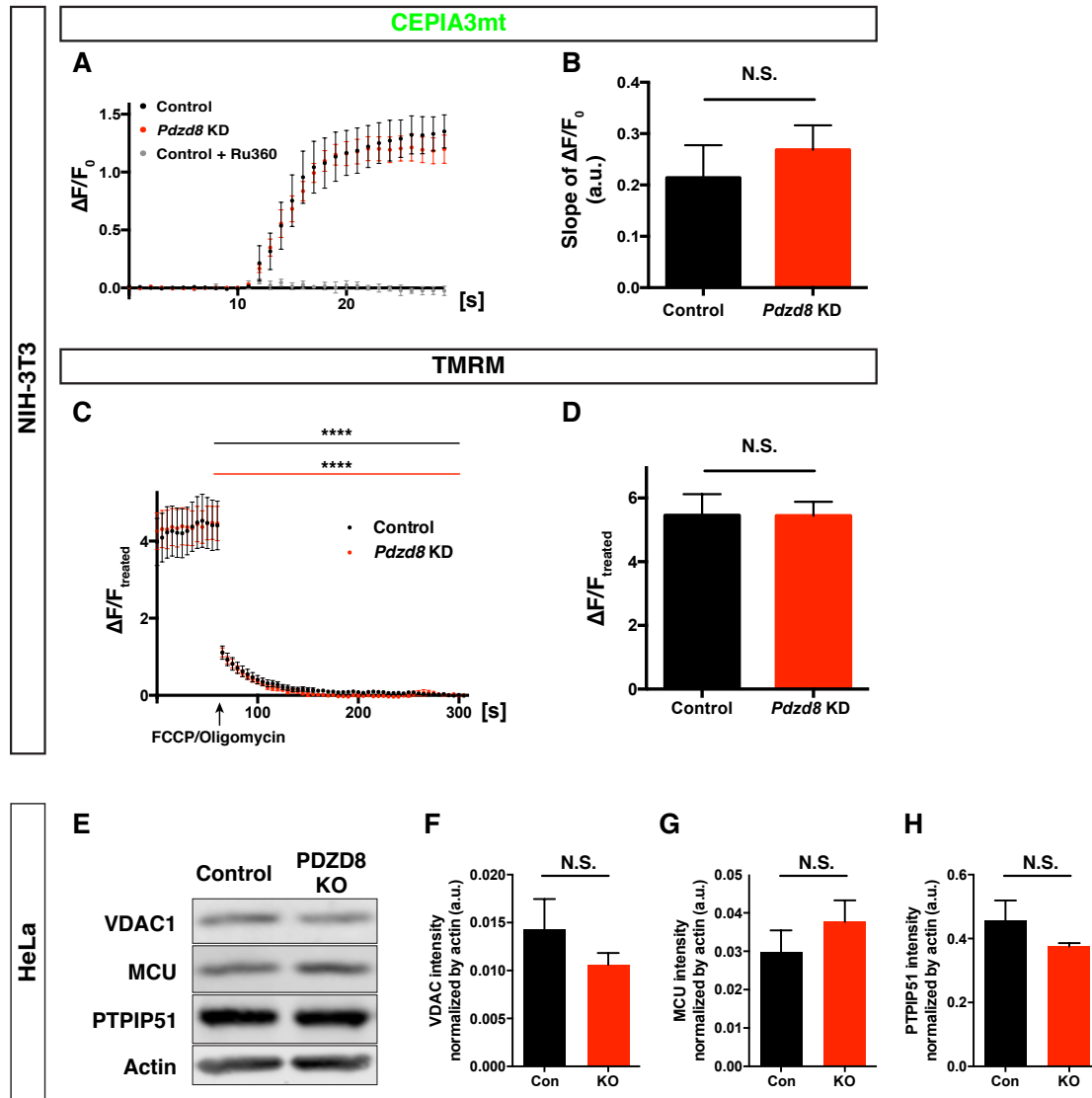
Fig. S9 Mitochondrial Ca²⁺ import machinery, membrane potential and other MAM proteins are not altered in PDZD8-depleted mammalian cells.

(**A-B**) Mitochondrial Ca²⁺ uptake itself is intact in PDZD8 KD NIH3T3 cells. NIH3T3 cells expressing CEPIA3mt were permeabilized with 2.5 μM digitonin and treated with SERCA inhibitor (CPA 20 μM) for 3 min allowing to measure directly mitochondrial Ca²⁺ uptake following application of 1mM Ca²⁺ (at 10sec). This uptake is purely dependent of MCU because it is completely abolished by application of MCU inhibitor (Ru360, 10μM). Slope of $\Delta F/F_0$ increase in the linear phase was calculated as an indicator for the speed of mitochondrial Ca²⁺ uptake which is dependent on combination of MCU expression level and MCU channel gating properties. The uptake speed was not significantly different between the control and *Pdzd8* KD cell. n= 9 (Control), 12 (*Pdzd8* KD). Mann-Whitney test. (**C-D**) Mitochondrial membrane potential is maintained in *Pdzd8* KD NIH3T3 cells. NIH3T3 cells expressing mito-YFP and either control or shPdzd8 plasmids were loaded with 20 nM TMRM for 20 min and were imaged for 1min

in the presence of 5 nM TMRM. Then, cells were treated with 0.3 μM FCCP (electron transport chain uncoupler) and 1μg/μl Oligomycin (ATPase blocker) for complete elimination of mitochondrial potential (used as baseline fluorescence for normalization). (C) Changes of TMRM fluorescence (ΔF). ****$p<0.0001$ according to paired t-test. (D) Mitochondrial TMRM signals normalized by baseline show no difference between control and *Pdzd8* KD cells. n= 17 (Control), 16 (*Pdzd8* KD). Mann-Whitney test. (**E-H**) Expression of mitochondrial Ca^{2+} regulatory proteins and other tethering proteins are not changed in PDZD8 KO HeLa cells. Immunoblot of control and PDZD8 KO HeLa cells shows no significant difference in expression level of mitochondrial Ca^{2+} uptake proteins (VDAC1 and MCU) and other ER/mitochondria tethering components (PTPIP51 and VDAC1). n=3 blots, Mann-Whitney test.
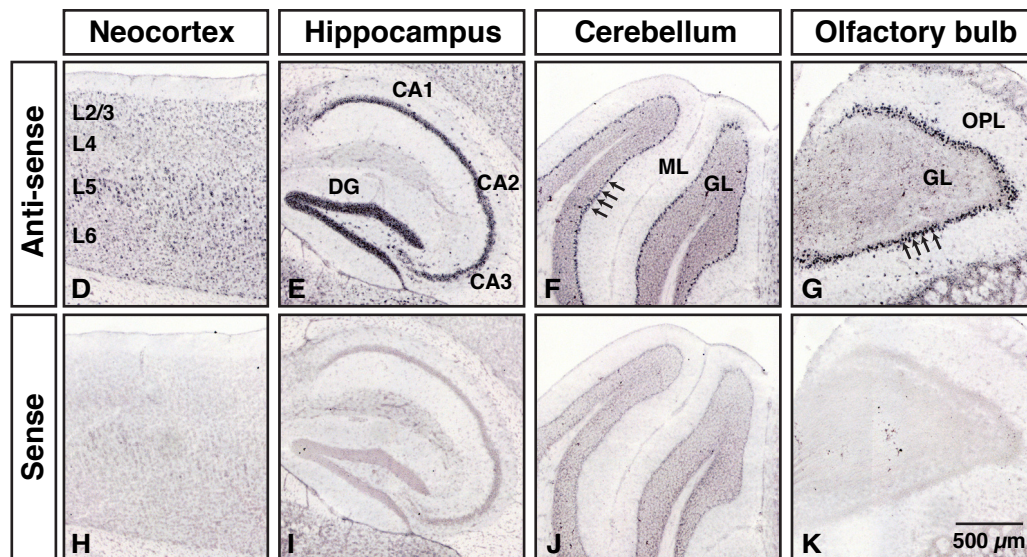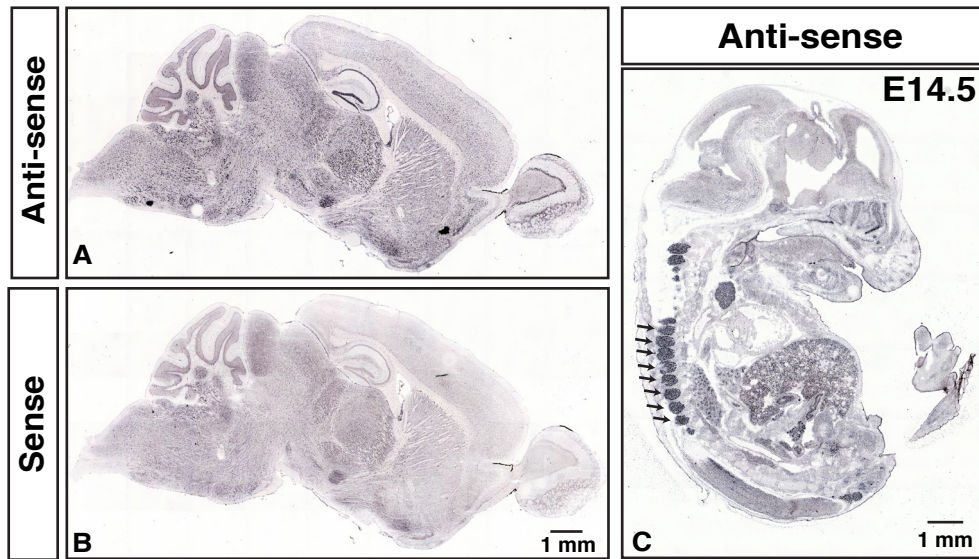
Fig. S10 *In situ* hybridization for *Pdzd8* mRNA in the embryonic and adult mouse brain.

Sections from brains of adult (A, B, D-K) or E14.5 C57Bl6 mouse embryos (C) were hybridized with either antisense (A, C, D-G) or sense probes (negative control, B, H-K) for mouse *Pdzd8* mRNA. (A, B) Sagittal sections of adult brains. (C) Sagittal section of E14.5 embryo. (D-K) Regions of brain indicated. Arrows indicate dorsal root ganglia in (C), Purkinje cells in (F), and mitral cells in (G).

Abbreviations: L, Layer; DG, Dentate gyrus; ML, Molecular layer; GL, Granule layer; OPL, Outer Plexiform Layer.
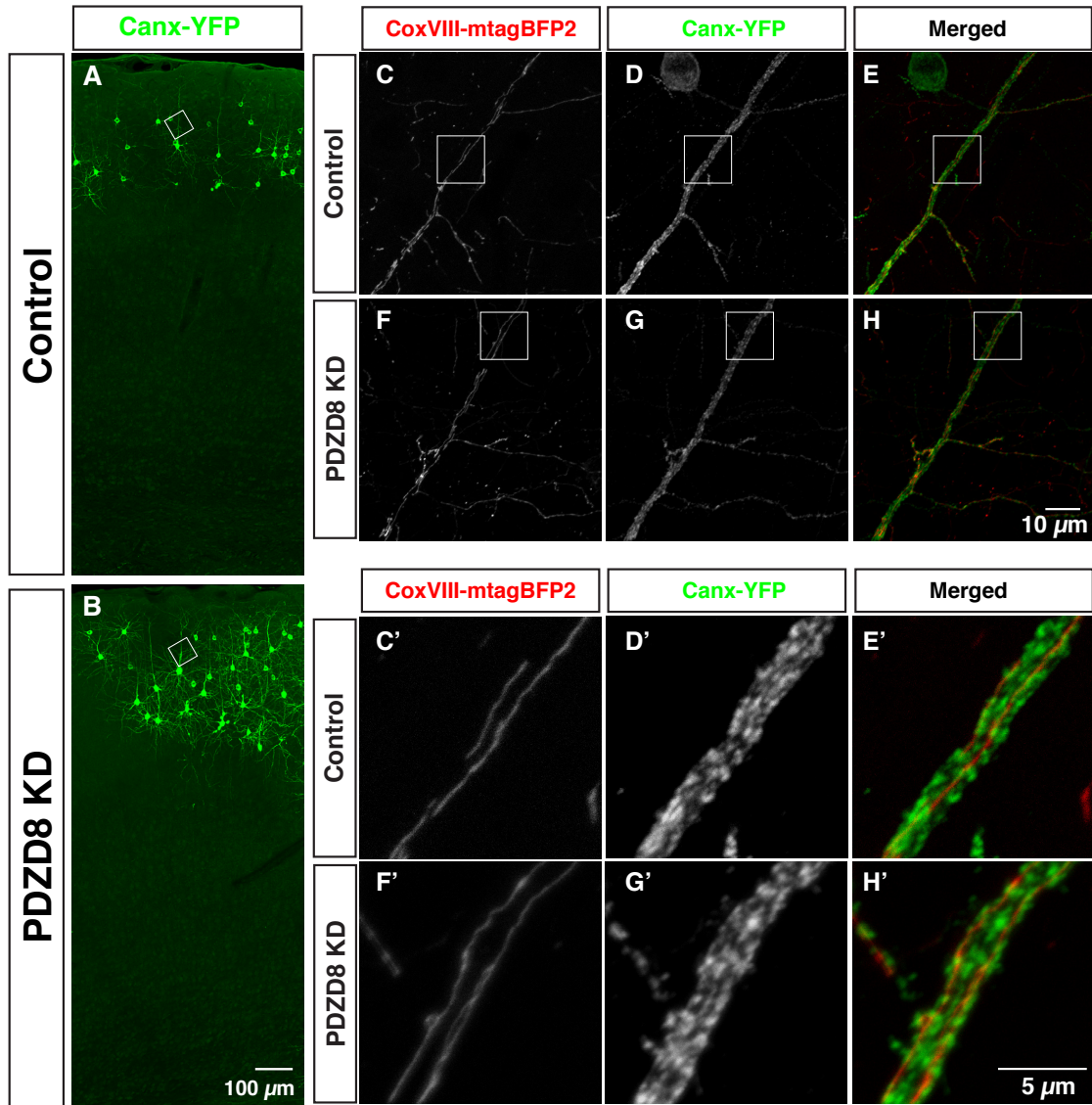
Fig. S11 Normal structure and distribution of mitochondria and ER in dendrites of control and PDZD8-depleted layer 2/3 pyramidal neurons *in vivo*.

Plasmids expressing COXVIII-mtagBFP2 (mitochondrial marker) and Canx-YFP (ER marker) with either control shRNA or *Pdzd8* shRNA were electroporated into the neocortex using *in utero* cortical electroporation at E15.5 and examined by confocal microscopy at P21. The apical dendrites of layer 2/3 neurons in the primary somatosensory cortex (S1) were imaged (A, B). The squares in panels A-B indicate the regions shown at high magnification in C-H. The squares in C-H indicate the regions shown at high magnification in C'-H'. Maximum projection images from 7.2 μm (C-E), 3.5 μm (C'-E'), 13.6 μm (F-H), and 4.25 μm (F'-H') thick Z-stacks are shown.
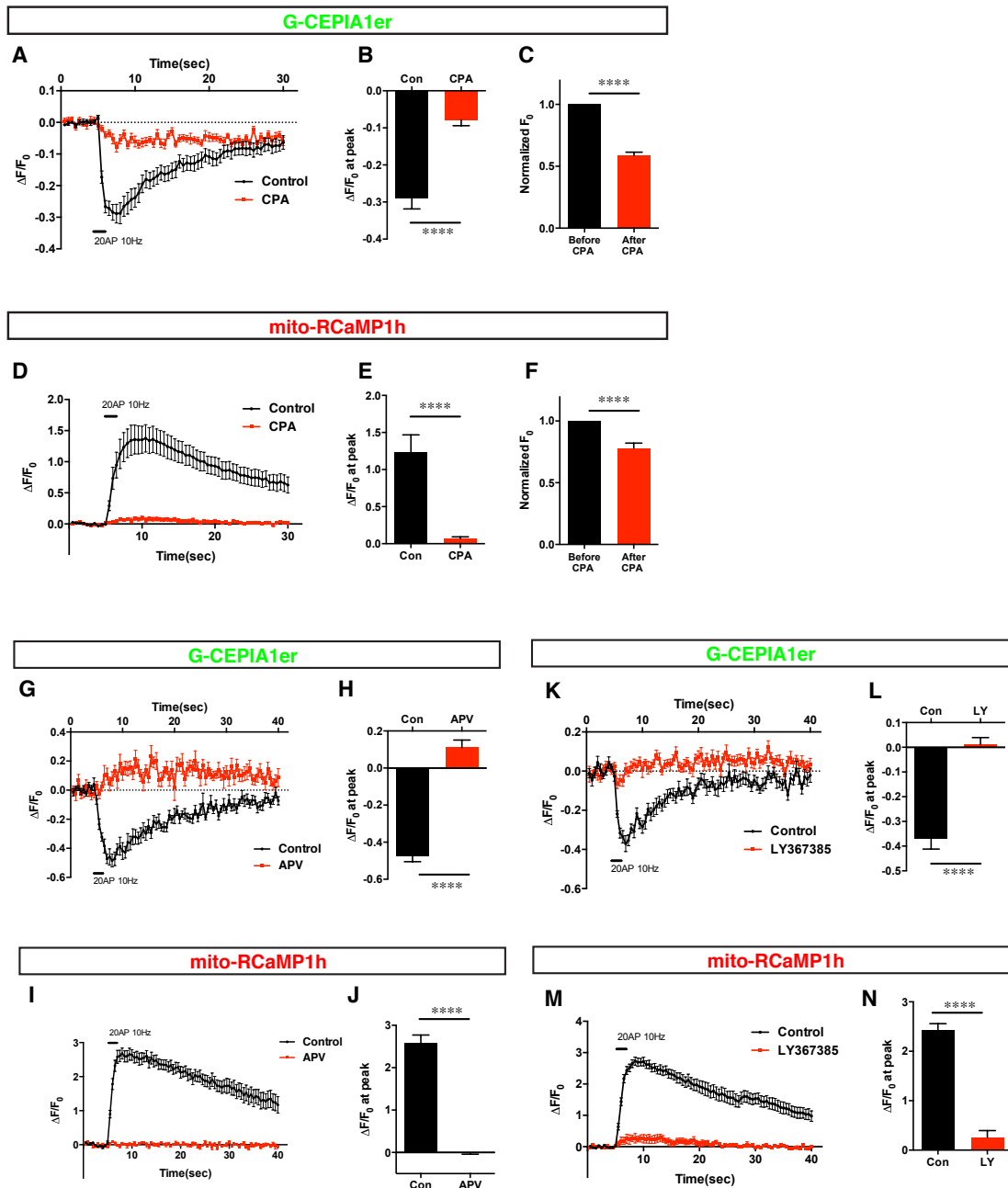
Fig. S12 Pharmacological dissection of ER-mitochondria Ca²⁺ exchange evoked by synaptic stimulation in cortical pyramidal neurons.

(**A-F**) ER Ca²⁺-depletion disrupts mitochondrial Ca²⁺ elevation during repetitive stimulation with 20APs at 10Hz. ER and mitochondrial Ca²⁺ dynamics were monitored using G-CEPIA1er and mito-RCaMP1h from the same cortical neurons (19-24DIV) before and after cyclopiazonic acid treatment (CPA, 30μM over 5min), which inhibits sarco/endoplasmic reticulum Ca²⁺-ATPase (SERCA). Inhibition of ER Ca²⁺ uptake blocks the replenishment of ER Ca²⁺ amount. Basal level of ER and mitochondrial Ca²⁺ is decreased after CPA treatment (C, F). This suggests that CPA treatment did not indirectly saturate mitochondrial Ca²⁺ concentration through store-operated Ca²⁺ entry (SOCE) in

dendrites. The modest but significant decreased in basal mitochondrial Ca^{2+} levels following CPA treatment cannot explain the almost complete disappearance of stimulation evoked mitochondrial Ca^{2+} increase observed in A-B. n=27 dendritic segments from 9 neurons. ****p<0.0001, Wilcoxon matched pairs signed rank test. (**G-J**) NMDA receptor-dependent Ca^{2+} influx is required for triggering ER Ca^{2+} release and mitochondrial Ca^{2+} influx upon stimulation with 20APs-10Hz. Neurons were imaged before and after NMDA receptor blocker, APV, application (50μM). APV treatment abolished ER Ca^{2+} release (G, H) and mitochondrial Ca^{2+} increase (I, J). n=16 dendritic segments from 5 neurons. ****p<0.0001, Paired t test. (**K-N**) Acute inhibition of mGluR1 by LY367385 (100μM applied 10 min before and during imaging) disrupts ER Ca^{2+} release and mitochondrial Ca^{2+} uptake during synaptic stimulation (20APs at 10Hz). n=22 dendritic segments from 8 neurons. ****p<0.0001, Wilcoxon matched pairs signed rank test.
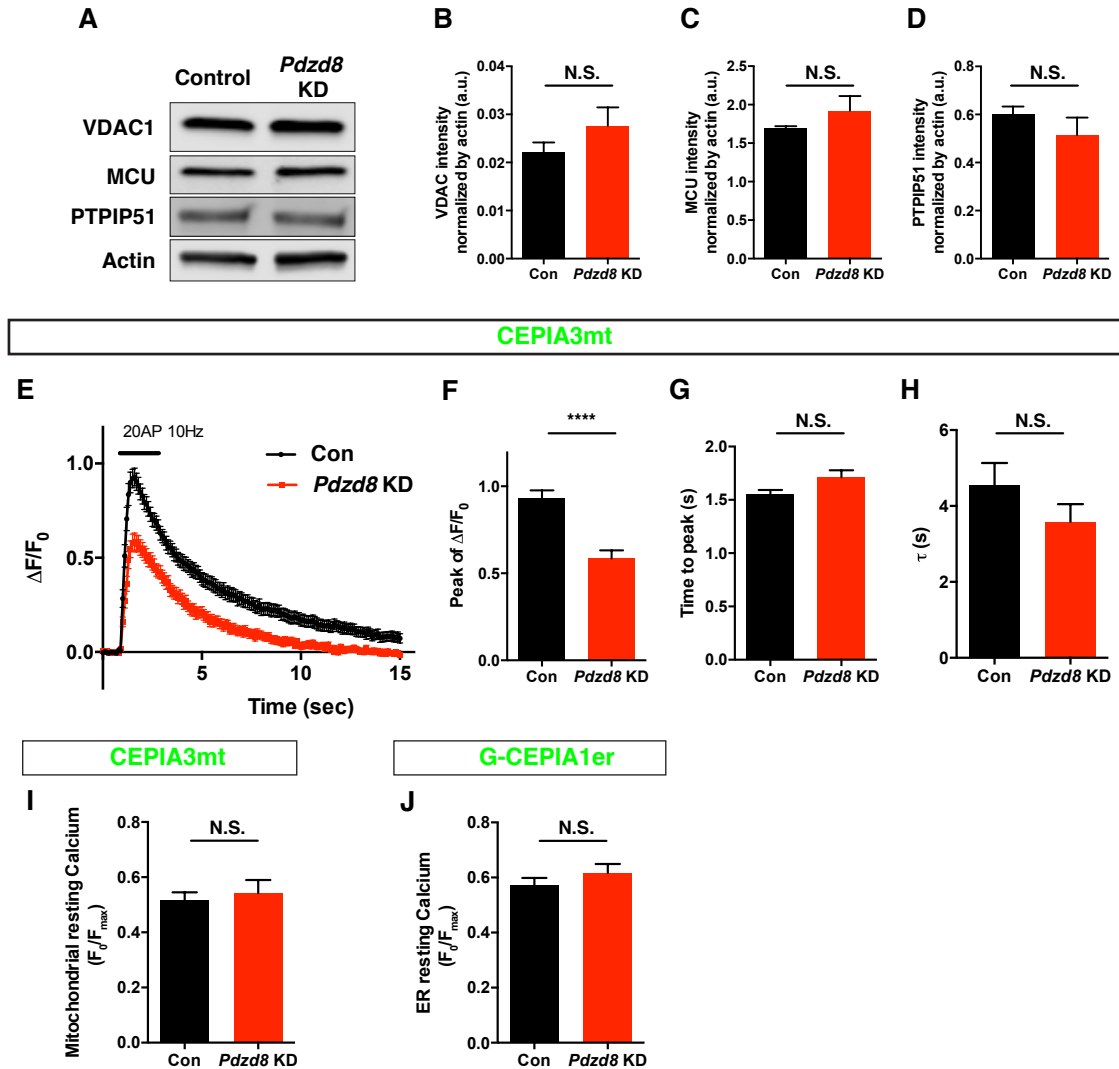
Fig. S13 Mitochondrial Ca²⁺ import machinery and other tethering components are not altered in *Pdzd8* knockdown cortical neurons.

(**A-D**) Expression of mitochondrial Ca²⁺ regulatory proteins and other tethering proteins are not changed in *Pdzd8* KD neurons. Cultured neurons were infected at 4DIV with lentivirus expressing either control shRNA or *Pdzd8* shRNA and cells were lysed at 14DIV. Immunoblot of control and PDZD8 KO neurons shows no difference in expression level of mitochondrial Ca²⁺ uptake proteins (VDAC1 and MCU) and other ER-mitochondria tethering components (PTPIP51 and VDAC1; n=3 independent immunoblots). (**E-H**) Mitochondrial Ca²⁺ uptake and extrusion kinetics are not affected by *Pdzd8* KD. Mitochondrial Ca²⁺ dynamics was monitored using CEPIA3mt at 21-22DIV with 20APs. We employed CEPIA3mt for measuring more precisely mitochondrial Ca²⁺ kinetics because of its lower Ca²⁺ affinity (K_d=11μM) compared to mito-RCaMPh1 (K_d=1.3μM), and thus to minimize saturation in some cells following synaptic stimulation. Images were captured with 100ms interval. Time to peak and decay time constant (τ) are not altered in dendrites of *Pdzd8* KD neurons compared to control

neurons, but peak of the CEPIA3mt signals is significantly reduced (by ~40%). n= 57 dendritic segments from 26 neurons for control, and 67 dendritic segments from 27 neurons for *Pdzd8* KD. (**I-J**) Resting level Ca^{2+} of mitochondria and ER are not changed in *Pdzd8* KD neurons. Somatic CEPIA3mt and dendritic G-CEPIA1er signals were measured before (for F_0) and after ionomycin treatment (for F_{max}). Normalized baseline signals (F_0/ F_{max}) showed no significant difference between control and PDZD8-deficient neurons. n=7 neurons for control and 9 neurons for *Pdzd8* KD in somatic CEPIA3mt analysis. n=38 dendritic segments from 14 neurons for control and 32 dendritic segments from 13 neurons for *Pdzd8* KD in dendritic G-GCEPIA1er analysis. Statistical significance: n.s. $p>0.05$, ****$p<0.0001$ according to non-parametric Mann-Whitney test.

Captions for Movies S1-S9

Movie S1. Serial z-stack images of Pdzd8-venus knock-in N2a cells.
The cell shown in Figures 1 and S6 (E-H) was imaged using 3D N-SIM (step size 0.12 μm, 20 sections) showing predominant colocalization of PDZD8-Venus with ER (red, Calnexin-mCherry). See legend of Figure 1 for details.

Movies S2 and S3. 3D FIB-SEM image series and animation showing reconstructed ER, mitochondria and ER-mitochondria contacts of control HeLa cells.
Serial EM images (20 nm interval, 100 sections for Movie 2, 83 sections for Movie 3) from areas enriched with sheet-like ER (**Movie 2**) or tubular ER (**Movie 3**), obtained by FIB-SEM of control HeLa cells are shown. The mitochondria and ER were labeled with green and magenta, respectively. This is merged with the 3-dimensional distribution of mitochondria (green) and ER (magenta), followed by display of only ER-mitochondria contact sites labeled in magenta on the last frames. See text for details.

Movies S4 and S5. 3D-SEM image series and animation showing reconstructed ER, mitochondria and ER-mitochondria contacts in PDZD8 KO HeLa cells.
Serial FIB-SEM images (20 nm interval, 38 sections for Movie 4, 75 sections for Movie 5) from areas enriched with sheet-like ER (**Movie 4**) or tubular ER (**Movie 5**) obtained by FIB-SEM of PDZD8-KO HeLa cells are shown. The mitochondria and ER were labeled with green and magenta, respectively. This is merged with the 3-dimensional distribution of mitochondria (green) and ER (magenta), followed by display of only ER-mitochondria contact sites labeled in magenta on the last frames. See text for details.

Movie S6. ATP-induced Ca^{2+} release from ER and transfer into mitochondria in control NIH3T3 cells.
Representative time-lapse images of ER and mitochondrial Ca^{2+} dynamics before and after ATP stimulation. Cells are displayed in ratio view normalized by basal signals (F_0) of each probe using R-CEPIA1er and G-CEPIA3mt. F/F_0 values are plotted for the duration of the acquisition. See text for details.

Movie. S7 ATP-induced Ca²⁺ release from ER and transfer into mitochondria in *Pdzd8* KD NIH3T3 cells.
Representative time-lapse images of ER and mitochondrial Ca^{2+} dynamics before and after ATP stimulation. Color range displayed as ratio of fluorescence value (F) normalized by basal signals (F_0) of each probe (R-CEPIA1er and CEPIA3mt). Bottom panels: F/F_0 values are plotted for the duration of the acquisition. See text for details.

Movie. S8 Ca²⁺ transfer from ER to mitochondria upon synaptic stimulation in proximal dendrites of cortical pyramidal neuron expressing control shRNA.
Representative time-lapse images of ER and mitochondrial Ca^{2+} dynamics before and after synaptic stimulation (20AP, 10Hz) in cortical neurons expressing control shRNA. Color range displayed as ratio of fluorescence values (F) normalized by basal signals (F_0) for each probe (G-CEPIA1er and mito-RCaMP1h). Bottom panels: F/F_0 values are plotted for the duration of the acquisition. See text for details.

Movie. S9 Ca²⁺ transfer from ER to mitochondria upon synaptic stimulation in proximal dendrite of cortical pyramidal neuron expressing *Pdzd8* shRNA.
Representative time-lapse images of ER and mitochondrial Ca^{2+} dynamics before and after synaptic stimulation (20AP, 10Hz) expressing *Pdzd8* shRNA. Color range displayed as ratio view normalized by basal signals (F/F_0) for each probe (G-CEPIA1er and mito-RCaMP1h). Bottom panels: F/F_0 values are plotted for the duration of the acquisition. See text for details.

References

1. B. Kornmann, E. Currie, S. R. Collins, M. Schuldiner, J. Nunnari, J. S. Weissman, P. Walter, An ER-mitochondria tethering complex revealed by a synthetic biology screen. *Science* **325**, 477–481 (2009). doi:10.1126/science.1175088 Medline

2. R. Rizzuto, P. Pinton, W. Carrington, F. S. Fay, K. E. Fogarty, L. M. Lifshitz, R. A. Tuft, T. Pozzan, Close contacts with the endoplasmic reticulum as determinants of mitochondrial Ca2+ responses. *Science* **280**, 1763–1766 (1998). doi:10.1126/science.280.5370.1763 Medline

3. E. Area-Gomez, A. J. C. de Groof, I. Boldogh, T. D. Bird, G. E. Gibson, C. M. Koehler, W. H. Yu, K. E. Duff, M. P. Yaffe, L. A. Pon, E. A. Schon, Presenilins are enriched in endoplasmic reticulum membranes associated with mitochondria. *Am. J. Pathol.* **175**, 1810–1816 (2009). doi:10.2353/ajpath.2009.090219 Medline

4. E. Area-Gomez, E. A. Schon, Mitochondria-associated ER membranes and Alzheimer disease. *Curr. Opin. Genet. Dev.* **38**, 90–96 (2016). doi:10.1016/j.gde.2016.04.006 Medline

5. S. Paillusson, R. Stoica, P. Gomez-Suaga, D. H. W. Lau, S. Mueller, T. Miller, C. C. J. Miller, There's something wrong with my MAM; the ER-mitochondria axis and neurodegenerative diseases. *Trends Neurosci.* **39**, 146–157 (2016). doi:10.1016/j.tins.2016.01.008 Medline

6. O. M. de Brito, L. Scorrano, Mitofusin 2 tethers endoplasmic reticulum to mitochondria. *Nature* **456**, 605–610 (2008). doi:10.1038/nature07534 Medline

7. G. Szabadkai, K. Bianchi, P. Várnai, D. De Stefani, M. R. Wieckowski, D. Cavagna, A. I. Nagy, T. Balla, R. Rizzuto, Chaperone-mediated coupling of endoplasmic reticulum and mitochondrial Ca2+ channels. *J. Cell Biol.* **175**, 901–911 (2006). doi:10.1083/jcb.200608073 Medline

8. K. J. De Vos, G. M. Mórotz, R. Stoica, E. L. Tudor, K.-F. Lau, S. Ackerley, A. Warley, C. E. Shaw, C. C. J. Miller, VAPB interacts with the mitochondrial protein PTPIP51 to regulate calcium homeostasis. *Hum. Mol. Genet.* **21**, 1299–1311 (2012). doi:10.1093/hmg/ddr559 Medline

9. Y. Lim, I. T. Cho, L. J. Schoel, G. Cho, J. A. Golden, Hereditary spastic paraplegia-linked REEP1 modulates endoplasmic reticulum/mitochondria contacts. *Ann. Neurol.* **78**, 679–696 (2015). doi:10.1002/ana.24488 Medline

10. P. Cosson, A. Marchetti, M. Ravazzola, L. Orci, Mitofusin-2 independent juxtaposition of endoplasmic reticulum and mitochondria: An ultrastructural study. *PLOS ONE* **7**, e46293 (2012). doi:10.1371/journal.pone.0046293 Medline

11. R. Filadi, E. Greotti, G. Turacchio, A. Luini, T. Pozzan, P. Pizzo, Mitofusin 2 ablation increases endoplasmic reticulum-mitochondria coupling. *Proc. Natl. Acad. Sci. U.S.A.* **112**, E2174–E2181 (2015). doi:10.1073/pnas.1504880112 Medline

12. D. Naon, M. Zaninello, M. Giacomello, T. Varanita, F. Grespi, S. Lakshminaranayan, A. Serafini, M. Semenzato, S. Herkenne, M. I. Hernández-Alvarez, A. Zorzano, D. De Stefani, G. W. Dorn 2nd, L. Scorrano, Critical reappraisal confirms that mitofusin 2 is an endoplasmic reticulum-mitochondria tether. *Proc. Natl. Acad. Sci. U.S.A.* **113**, 11249–11254 (2016). doi:10.1073/pnas.1606786113 Medline

13. A. P. AhYoung, J. Jiang, J. Zhang, X. Khoi Dang, J. A. Loo, Z. H. Zhou, P. F. Egea, Conserved SMP domains of the ERMES complex bind phospholipids and mediate tether assembly. *Proc. Natl. Acad. Sci. U.S.A.* **112**, E3179–E3188 (2015). doi:10.1073/pnas.1422363112 Medline

14. C. M. Schauder, X. Wu, Y. Saheki, P. Narayanaswamy, F. Torta, M. R. Wenk, P. De Camilli, K. M. Reinisch, Structure of a lipid-bound extended synaptotagmin indicates a role in lipid transfer. *Nature* **510**, 552–555 (2014). doi:10.1038/nature13269 Medline

15. H. Jeong, J. Park, C. Lee, Crystal structure of Mdm12 reveals the architecture and dynamic organization of the ERMES complex. *EMBO Rep.* **17**, 1857–1871 (2016). doi:10.15252/embr.201642706 Medline

16. S. C. Helle, G. Kanfer, K. Kolar, A. Lang, A. H. Michel, B. Kornmann, Organization and function of membrane contact sites. *Biochim. Biophys. Acta* **1833**, 2526–2541 (2013). doi:10.1016/j.bbamcr.2013.01.028 Medline

17. V. Alva, A. N. Lupas, The TULIP superfamily of eukaryotic lipid-binding proteins as a mediator of lipid sensing and transport. *Biochim. Biophys. Acta* **1861**, 913–923 (2016). doi:10.1016/j.bbalip.2016.01.016 Medline

18. K. O. Kopec, V. Alva, A. N. Lupas, Homology of SMP domains to the TULIP superfamily of lipid-binding proteins provides a structural basis for lipid exchange between ER and mitochondria. *Bioinformatics* **26**, 1927–1931 (2010). doi:10.1093/bioinformatics/btq326 Medline

19. I. Lee, W. Hong, Diverse membrane-associated proteins contain a novel SMP domain. *FASEB J.* **20**, 202–206 (2006). doi:10.1096/fj.05-4581hyp Medline

20. B. Kornmann, P. Walter, ERMES-mediated ER-mitochondria contacts: Molecular hubs for the regulation of mitochondrial biology. *J. Cell Sci.* **123**, 1389–1393 (2010). doi:10.1242/jcs.058636 Medline

21. T. Hanekamp, M. K. Thorsness, I. Rebbapragada, E. M. Fisher, C. Seebart, M. R. Darland, J. A. Coxbill, D. L. Updike, P. E. Thorsness, Maintenance of mitochondrial morphology is linked to maintenance of the mitochondrial genome in *Saccharomyces cerevisiae*. *Genetics* **162**, 1147–1156 (2002). Medline

22. A. E. Hobbs, M. Srinivasan, J. M. McCaffery, R. E. Jensen, Mmm1p, a mitochondrial outer membrane protein, is connected to mitochondrial DNA (mtDNA) nucleoids and required for mtDNA stability. *J. Cell Biol.* **152**, 401–410 (2001). doi:10.1083/jcb.152.2.401 Medline

23. A. B. Lang, A. T. John Peter, P. Walter, B. Kornmann, ER-mitochondrial junctions can be bypassed by dominant mutations in the endosomal protein Vps13. *J. Cell Biol.* **210**, 883–890 (2015). doi:10.1083/jcb.201502105 Medline

24. S. Zhang, J. Sodroski, Efficient human immunodeficiency virus (HIV-1) infection of cells lacking PDZD8. *Virology* **481**, 73–78 (2015). doi:10.1016/j.virol.2015.01.034 Medline

25. L. M. Westrate, J. E. Lee, W. A. Prinz, G. K. Voeltz, Form follows function: The importance of endoplasmic reticulum shape. *Annu. Rev. Biochem.* **84**, 791–811 (2015). doi:10.1146/annurev-biochem-072711-163501 Medline

26. S. Chen, T. Desai, J. A. McNew, P. Gerard, P. J. Novick, S. Ferro-Novick, Lunapark stabilizes nascent three-way junctions in the endoplasmic reticulum. *Proc. Natl. Acad. Sci. U.S.A.* **112**, 418–423 (2015). doi:10.1073/pnas.1423026112 Medline

27. R. Stoica, K. J. De Vos, S. Paillusson, S. Mueller, R. M. Sancho, K.-F. Lau, G. Vizcay-Barrena, W.-L. Lin, Y.-F. Xu, J. Lewis, D. W. Dickson, L. Petrucelli, J. C. Mitchell, C. E. Shaw, C. C. J. Miller, ER-mitochondria associations are regulated by the VAPB-PTPIP51 interaction and are disrupted by ALS/FTD-associated TDP-43. *Nat. Commun.* **5**, 3996 (2014). doi:10.1038/ncomms4996 Medline

28. G. Csordás, C. Renken, P. Várnai, L. Walter, D. Weaver, K. F. Buttle, T. Balla, C. A. Mannella, G. Hajnóczky, Structural and functional features and significance of the physical linkage between ER and mitochondria. *J. Cell Biol.* **174**, 915–921 (2006). doi:10.1083/jcb.200604016 Medline

29. A. A. Rowland, G. K. Voeltz, Endoplasmic reticulum-mitochondria contacts: Function of the junction. *Nat. Rev. Mol. Cell Biol.* **13**, 607–625 (2012). doi:10.1038/nrm3440 Medline

30. M. Giacomello, I. Drago, M. Bortolozzi, M. Scorzeto, A. Gianelle, P. Pizzo, T. Pozzan, Ca2+ hot spots on the mitochondrial surface are generated by Ca2+ mobilization from stores, but not by activation of store-operated Ca2+ channels. *Mol. Cell* **38**, 280–290 (2010). doi:10.1016/j.molcel.2010.04.003 Medline

31. G. Csordás, P. Várnai, T. Golenár, S. Roy, G. Purkins, T. G. Schneider, T. Balla, G. Hajnóczky, Imaging interorganelle contacts and local calcium dynamics at the ER-mitochondrial interface. *Mol. Cell* **39**, 121–132 (2010). doi:10.1016/j.molcel.2010.06.029 Medline

32. M. Patron, V. Checchetto, A. Raffaello, E. Teardo, D. Vecellio Reane, M. Mantoan, V. Granatiero, I. Szabò, D. De Stefani, R. Rizzuto, MICU1 and MICU2 finely tune the mitochondrial Ca2+ uniporter by exerting opposite effects on MCU activity. *Mol. Cell* **53**, 726–737 (2014). doi:10.1016/j.molcel.2014.01.013 Medline

33. J. Suzuki, K. Kanemaru, K. Ishii, M. Ohkura, Y. Okubo, M. Iino, Imaging intraorganellar Ca2+ at subcellular resolution using CEPIA. *Nat. Commun.* **5**, 4153 (2014). doi:10.1038/ncomms5153 Medline

34. G. Burnstock, Purine and pyrimidine receptors. *Cell. Mol. Life Sci.* **64**, 1471–1483 (2007). doi:10.1007/s00018-007-6497-0 Medline

35. N. Spruston, Pyramidal neurons: Dendritic structure and synaptic integration. *Nat. Rev. Neurosci.* **9**, 206–221 (2008). doi:10.1038/nrn2286 Medline

36. P. J. Sjöström, E. A. Rancz, A. Roth, M. Häusser, Dendritic excitability and synaptic plasticity. *Physiol. Rev.* **88**, 769–840 (2008). doi:10.1152/physrev.00016.2007 Medline

37. S. H. Lee, K.-R. Kim, S.-Y. Ryu, S. Son, H. S. Hong, I. Mook-Jung, S.-H. Lee, W.-K. Ho, Impaired short-term plasticity in mossy fiber synapses caused by mitochondrial dysfunction of dentate granule cells is the earliest synaptic deficit in a mouse model of Alzheimer's disease. *J. Neurosci.* **32**, 5953–5963 (2012). doi:10.1523/JNEUROSCI.0465-12.2012 Medline

38. S. A. Thayer, R. J. Miller, Regulation of the intracellular free calcium concentration in single rat dorsal root ganglion neurones in vitro. *J. Physiol.* **425**, 85–115 (1990). doi:10.1113/jphysiol.1990.sp018094 Medline

39. S. J. Cherra 3rd, E. Steer, A. M. Gusdon, K. Kiselyov, C. T. Chu, Mutant LRRK2 elicits calcium imbalance and depletion of dendritic mitochondria in neurons. *Am. J. Pathol.* **182**, 474–484 (2013). doi:10.1016/j.ajpath.2012.10.027 Medline

40. M. F. Yeckel, A. Kapur, D. Johnston, Multiple forms of LTP in hippocampal CA3 neurons use a common postsynaptic mechanism. *Nat. Neurosci.* **2**, 625–633 (1999). doi:10.1038/10180 Medline

41. N. Emptage, T. V. Bliss, A. Fine, Single synaptic events evoke NMDA receptor-mediated release of calcium from internal stores in hippocampal dendritic spines. *Neuron* **22**, 115–124 (1999). doi:10.1016/S0896-6273(00)80683-2 Medline

42. M. Nishiyama, K. Hong, K. Mikoshiba, M. M. Poo, K. Kato, Calcium stores regulate the polarity and input specificity of synaptic modification. *Nature* **408**, 584–588 (2000). doi:10.1038/35046067 Medline

43. E. A. Finch, G. J. Augustine, Local calcium signalling by inositol-1,4,5-trisphosphate in Purkinje cell dendrites. *Nature* **396**, 753–756 (1998). doi:10.1038/25541 Medline

44. H. Takechi, J. Eilers, A. Konnerth, A new class of synaptic response involving calcium release in dendritic spines. *Nature* **396**, 757–760 (1998). doi:10.1038/25547 Medline

45. S. S. Wang, W. Denk, M. Häusser, Coincidence detection in single dendritic spines mediated by calcium release. *Nat. Neurosci.* **3**, 1266–1273 (2000). doi:10.1038/81792 Medline

46. M. Miyata, E. A. Finch, L. Khiroug, K. Hashimoto, S. Hayasaka, S.-I. Oda, M. Inouye, Y. Takagishi, G. J. Augustine, M. Kano, Local calcium release in dendritic spines required for long-term synaptic depression. *Neuron* **28**, 233–244 (2000). doi:10.1016/S0896-6273(00)00099-4 Medline

47. K. F. Lee, C. Soares, J. P. Thivierge, J. C. Béïque, Correlated synaptic inputs drive dendritic calcium amplification and cooperative plasticity during clustered synapse development. *Neuron* **89**, 784–799 (2016). doi:10.1016/j.neuron.2016.01.012 Medline

48. J. Akerboom, N. Carreras Calderón, L. Tian, S. Wabnig, M. Prigge, J. Tolö, A. Gordus, M. B. Orger, K. E. Severi, J. J. Macklin, R. Patel, S. R. Pulver, T. J. Wardill, E. Fischer, C. Schüler, T.-W. Chen, K. S. Sarkisyan, J. S. Marvin, C. I. Bargmann, D. S. Kim, S. Kügler, L. Lagnado, P. Hegemann, A. Gottschalk, E. R. Schreiter, L. L. Looger, Genetically encoded calcium indicators for multi-color neural activity imaging and combination with optogenetics. *Front. Mol. Neurosci.* **6**, 2 (2013). doi:10.3389/fnmol.2013.00002 Medline

49. A. Maximov, Z. P. Pang, D. G. Tervo, T. C. Südhof, Monitoring synaptic transmission in primary neuronal cultures using local extracellular stimulation. *J. Neurosci. Methods* **161**, 75–87 (2007). doi:10.1016/j.jneumeth.2006.10.009 Medline

50. A. Verkhratsky, Physiology and pathophysiology of the calcium store in the endoplasmic reticulum of neurons. *Physiol. Rev.* **85**, 201–279 (2005). doi:10.1152/physrev.00004.2004 Medline

51. A. Losonczy, J. K. Makara, J. C. Magee, Compartmentalized dendritic plasticity and input feature storage in neurons. *Nature* **452**, 436–441 (2008). doi:10.1038/nature06725 Medline

52. M. E. Sheffield, D. A. Dombeck, Calcium transient prevalence across the dendritic arbour predicts place field properties. *Nature* **517**, 200–204 (2015). doi:10.1038/nature13871 Medline

53. T. L. Lewis Jr., G. F. Turi, S. K. Kwon, A. Losonczy, F. Polleux, Progressive decrease of mitochondrial motility during maturation of cortical axons in vitro and in vivo. *Curr. Biol.* **26**, 2602–2608 (2016). doi:10.1016/j.cub.2016.07.064 Medline

54. S. K. Kwon, R. Sando 3rd, T. L. Lewis, Y. Hirabayashi, A. Maximov, F. Polleux, LKB1 regulates mitochondria-dependent presynaptic calcium clearance and neurotransmitter release properties at excitatory synapses along cortical axons. *PLOS Biol.* **14**, e1002516 (2016). doi:10.1371/journal.pbio.1002516 Medline

55. F. A. Ran, P. D. Hsu, J. Wright, V. Agarwala, D. A. Scott, F. Zhang, Genome engineering using the CRISPR-Cas9 system. *Nat. Protoc.* **8**, 2281–2308 (2013). doi:10.1038/nprot.2013.143 Medline

56. L. A. Kelley, S. Mezulis, C. M. Yates, M. N. Wass, M. J. Sternberg, The Phyre2 web portal for protein modeling, prediction and analysis. *Nat. Protoc.* **10**, 845–858 (2015). doi:10.1038/nprot.2015.053 Medline

57. R. Gauss, M. Trautwein, T. Sommer, A. Spang, New modules for the repeated internal and N-terminal epitope tagging of genes in *Saccharomyces cerevisiae*. *Yeast* **22**, 1–12 (2005). doi:10.1002/yea.1187 Medline

58. F. Sherman, J. Hicks, Micromanipulation and dissection of asci. *Methods Enzymol.* **194**, 21–37 (1991). doi:10.1016/0076-6879(91)94005-W Medline

59. F. Sherman, Getting started with yeast. *Methods Enzymol.* **350**, 3–41 (2002). doi:10.1016/S0076-6879(02)50954-X Medline

60. M. R. Wieckowski, C. Giorgi, M. Lebiedzinska, J. Duszynski, P. Pinton, Isolation of mitochondria-associated membranes and mitochondria from animal tissues and cells. *Nat. Protoc.* **4**, 1582–1590 (2009). doi:10.1038/nprot.2009.151 Medline

61. J. E. Vance, Phospholipid synthesis in a membrane fraction associated with mitochondria. *J. Biol. Chem.* **265**, 7248–7256 (1990). Medline

62. J. C. Tapia, N. Kasthuri, K. J. Hayworth, R. Schalek, J. W. Lichtman, S. J. Smith, J. Buchanan, High-contrast en bloc staining of neuronal tissue for field emission scanning electron microscopy. *Nat. Protoc.* **7**, 193–206 (2012). doi:10.1038/nprot.2011.439 Medline

63. J. R. Kremer, D. N. Mastronarde, J. R. McIntosh, Computer visualization of three-dimensional image data using IMOD. *J. Struct. Biol.* **116**, 71–76 (1996). doi:10.1006/jsbi.1996.0013 Medline

64. M. B. Yaylaoglu, A. Titmus, A. Visel, G. Alvarez-Bolado, C. Thaller, G. Eichele, Comprehensive expression atlas of fibroblast growth factors and their receptors generated by a novel robotic in situ hybridization platform. *Dev. Dyn.* **234**, 371–386 (2005). doi:10.1002/dvdy.20441 Medline